Fast Upscaling of the Hydraulic Conductivity of Three-Dimensional Fractured Porous Rock for Reservoir Modeling

Tawfik Rajeh, Rachid Ababou, Manuel Marcoux, Israel Canamon Valera

Fast Upscaling of the Hydraulic Conductivity of Three-Dimensional Fractured Porous Rock for Reservoir Modeling

Tawfik Rajeh[1] · **Rachid Ababou**[1] · **Manuel Marcoux**[1] · **Israel Cañamon**[2]

Abstract A fast upscaling procedure for determining the equivalent hydraulic conductivity of a three-dimensional fractured rock is presented in this paper. A modified semi-analytical superposition method is developed to take into account, at the same time, the hydraulic conductivity of the porous matrix (K_M) and the fractures (K_F). The connectivity of the conductive fracture network is also taken into account. The upscaling approach has been validated by comparison with the hydraulic conductivity of synthetic samples calculated with full numerical procedures (flow simulations and averaging). The extended superposition approach is in good agreement with numerical results for infinite size fractures. For finite size fractures, an improved model that takes into account the connectivity of the fracture network through multiplicative connectiv-ity indexes determined empirically is proposed. This improved model is also in good agreement with the numerical results obtained for different configurations of fracture networks.

Keywords Fractured porous medium · Three-dimensional upscaling · Equivalent hydraulic conductivity · Numerical simulations · Darcy · Random fracture sets · Network connectivity

✉ Tawfik Rajeh
tawfikrajeh@gmail.com

[1] Institut de Mécanique des Fluides de Toulouse (IMFT), CNRS and Université de Toulouse, 2 Allée du professeur Camille Soula, 31400 Toulouse, France

[2] ETSI de Minas y Energía, Departamento de Ingeniería Geológica y Minera, Universidad Politécnica de Madrid, C./Ríos Rosas 21, 28003 Madrid, Spain

1 Introduction

Geologic formations are heterogeneous over a broad range of scales. Small-scale heterogeneity must be represented at some coarser scale for feasible yet accurate simulations of flow and transport phenomena in reservoirs. The key parameter for hydraulic simulation, the hydraulic conductivity, is upscaled to a coarser grid by assigning an equivalent conductivity K_{EQ} to each cell of the coarse grid. The equivalent hydraulic conductivity K_{EQ} should be distinguished from the effective hydraulic conductivity $K_{EFF.}$ The equivalent conductivity K_{EQ} can be defined for any finite domain with specific boundary conditions, based on equivalence criteria (as done later in this paper). The effective conductivity K_{EFF} is usually defined theoretically for infinite domain. In the case of a continuous heterogeneous porous medium, and assuming that the local conductivity $K(x,y,z)$ is modeled by a statistically homogeneous and ergodic random function of space, the quantities K_{EQ} and K_{EFF} coincide in the limit of infinite upscaling domain. In the remainder of this introduction, a brief literature review of basic theoretical results on conductivity upscaling for heterogeneous porous media will be presented. Secondly, some of the most common upscaling methods and algorithms available in the literature will be presented. Finally, a summary description of the organization of this paper will be provided.

Theoretical results on equivalent conductivity are found in the literature in two forms, as bounds or as analytical relations. For heterogeneous porous media, the equivalent hydraulic conductivity must satisfy two fundamental inequalities called "Wiener bounds" (Wiener 1912). These bounds have been demonstrated in many works (Wiener 1912; Cardwell and Parsons 1945; Matheron 1967; others). They are given by

$$K_H \leq K_{EQ} \leq K_A, \tag{1}$$

where K_A and K_H represent respectively the arithmetic and the harmonic mean of hydraulic conductivity.

Other narrower bounds (or tighter bounds)[1] have been obtained in the literature for the equivalent hydraulic conductivity, but their domain of applicability is usually restricted to particular types of spatial distribution or probability distribution of the heterogeneous conductivity. The most known are the "HS" bounds (Hashin and Shtrikman 1963), which are valid only for the case of isotropic binary media (as explained further below). These bounds are given by

$$K_A - \frac{f_1 f_0 (K_1 - K_0)^2}{(1 - f_0)K_0 + f_0 K_1} \leq K_{EQ} \leq K_A - \frac{f_1 f_0 (K_1 - K_0)^2}{(1 - f_1)K_1 + f_1 K_0}, \tag{2}$$

[1] The terms "narrow bounds" and "tight bounds" both refer to the case where the lower and upper bounds (K_{LOW} and K_{UP}) are relatively close to each other; obviously, the inequality becomes an equality in the ideal case of equal bounds ($K_{LOW} = K_{UP}$).

where the labels 0 and 1 refer to the two conductive media ("binary mixture"). Thus, K_0 and K_1 represent respectively the hydraulic conductivities of medium 0 and medium 1; f_0 and f_1 represent the volumetric fractions of the two media; and K_A and K_H are the arithmetic and harmonic means of the binary conductivity distribution.

These HS bounds are theoretically relevant only for isotropic binary media. A fractured porous medium may be modeled as a matrix/fracture binary medium; however, the conductive porous matrix "0" and the conductive fractures "1" do not constitute an isotropic mixture. In addition, even for the ideal case of isotropic binary mixtures, the HS bounds in Eq. (2) may be far apart from each other. To sum up, keeping in mind the objective of upscaling fractured porous media, the HS bounds have several limitations: the assumed isotropy of the binary medium (a theoretical limitation), and the possible lack of tightness of the bounds (a practical limitation).

Analytical expressions for the equivalent hydraulic conductivity have been obtained in the literature, but only for some limited types of heterogeneous media (spatially correlated heterogeneity), or only for special types of discontinuous fractured media. Thus, Matheron (1967) obtained an analytical relation for the macroscopic permeability of a continuous, randomly heterogeneous medium where the local permeability $K(\boldsymbol{x})$ is a random field, under additional hypotheses of statistical homogeneity, isotropy, and ergodicity.[2] More precisely, Matheron's expression is theoretically valid under several hypotheses: (i) Euclidean space is two-dimensional; (ii) the mean flow field is uniform; (iii) the spatial distribution of $K(x,y)$ is statistically invariant under $\pi/2$ rotations (which is implied by statistical isotropy); and finally (iv) the probability distributions of K/K_G and its inverse K_G/K should be identical.[3]

In particular, as a special case, Matheron's relation holds for two-dimensional isotropic spatial distribution of $K(x,y)$ in an infinite domain, provided that the probability density function (PDF) of $\ln(K)$ is symmetric (footnote 3). Matheron's relation is given by

$$K_{\mathrm{EQ}} = E(K)^{1/2}\left[E(K^{-1})\right]^{-(1/2)}, \tag{3}$$

[2] *Homogeneity, ergodicity, isotropy*. A random field, such as $K(\boldsymbol{x})$ or $\ln K(\boldsymbol{x})$, is a random function of position ($\boldsymbol{x}$). The moments of a statistically homogeneous, or "stationary", random field are invariant by translation. Ergodicity refers to the convergence of spatial averages (spatial moments) to ensemble averages (ensemble moments), in the limit of infinite spatial domain. In practice, only the 1st and 2nd order moments are considered (2nd order stationarity and ergodicity). Finally, statistical isotropy refers to the case where the moments of the random field are invariant by rotation.

[3] *Probability distribution of a random field F(x).* One should distinguish the *single-point* probability law of $F(\mathbf{x})$, from its general *multipoint* probability law. In the case of a Gaussian random field, the one-point and two-point moments suffice to entirely define its *multipoint* probability law. In the two-dimensional case at hand, if $F = \ln K(x,y)$ is assumed Gaussian (in the sense "multi-Gaussian"), then $K(x,y)$ is by definition a "log-normal" random field. In that case, it can be shown that K/K_G and its inverse K_G/K both have well defined *multipoint* laws (log-normal) with the same moments. Furthermore, the mean, variance and two-point covariance of the log-normal $K(x,y)$ can be explicitly related to those of the Gaussian $\ln K(x,y)$.

where $E(K)$ is the mathematical expectation of K. If K is log-normal (that is, if $\ln K$ Gaussian, i.e., multi-Gaussian) then Eq. (3) specializes as: $K_{EQ} = \exp\{E(\ln K)\} = K_G$, which is the geometric mean of K. This relation is also applicable to two-dimensional networks of conductors (Marchant 1977). For more discussions on the probability distribution of K and its consequences, one can refer to Matheron (1967), Ababou et al. (1989) and Zinn and Harvey (2003), as well as the previous footnote. Note also that for a layered medium or for a porous medium containing a parallel set of fractures, the infinite domain equivalent conductivity is the arithmetic mean conductivity if the flow is parallel to the layers and the harmonic mean conductivity if the flow is perpendicular to layers. This classical result has been demonstrated and re-used by many authors since Wiener (1912).

Except for a few results such as those mentioned above, there is no analytical "formula" for determining the equivalent hydraulic conductivity of general three-dimensional fractured porous media, with planar disc fractures. However, many studies in recent decades have led to approximate methods for estimating the equivalent (upscaled) conductivity of a heterogeneous medium. Approximate upscaling methods do not require the direct numerical solution of the detailed equations governing flow in the heterogeneous medium, which are computationally very demanding in terms of CPU time and memory capacity. Indeed, direct numerical simulations require the discretization of the entire fractured porous domain (planar fractures and porous matrix), which leads to a great number of grid nodes or cells, because fracture apertures are very fine compared to porous matrix blocks or to fracture spacing. Among these approximate upscaling methods, the most popular are the self-consistent method (also known as effective medium theory), power averaging methods, and renormalization methods, among others.

The self-consistent method was introduced by Budiansky (1965) in a different context. Dagan (1979) applied the method for upscaling hydraulic conductivity in heterogeneous porous media. He considered a multiphase material made up of homogeneous blocks or "inclusions", with conductivities K_j ($j = 1,\ldots, N$). The blocks are distributed at random in a domain of infinite extent. The following expression was obtained for the effective hydraulic conductivity (Dagan 1979)

$$K_{EFF} + (m-1)\,K_M = \left[\int_0^\infty \frac{f(K)\,dK}{(m-1)K_{EFF} + K}\right]^{-1}, \tag{4}$$

where the unknown quantity is K_{EFF}, the effective conductivity of the random porous medium; K_M is the conductivity of the porous matrix; "m" is the dimension of Euclidean space ($m = 3$ for a three-dimensional problem); and $f(K)$ is the probability density function (PDF) of the random conductivity variable K. Note that the implicit relation in Eq. (4) must be solved or "inverted", for a given $f(K)$, in order to extract from it the effective conductivity K_{EFF}. This can be done analytically or numerically, depending on the probability law of K. The validity of the self-consistent Eq. (4) is limited due to some restrictive hypotheses and approximations. This relation was obtained by an approximate calculation of the pressure field around each "block", assuming that each block is spherical, and replacing the medium surrounding each block by a

homogeneous matrix having the (unknown) conductivity K_{EFF}. It is also assumed that the averaging volume is large compared to the single block inclusion. Pozdniakov and Tsang (2004) generalized the self-consistent method to ellipsoidal inclusions, which could represent fractures. More recently Sævik et al. (2013) proposed three varieties of the self-consistent formulation to ellipsoidal fractures. However, the self-consistent method provides a good estimation of K_{EFF} only in the case of poorly connected fractures or inclusions ("diluted limit").

On the other hand, several authors have proposed different types of power-averages to estimate the equivalent or the effective hydraulic conductivity of a heterogeneous medium. The power average is of the form: $K_{ii,\mathrm{EFF}} = \mathrm{E}(\mathrm{K}^{\mathrm{Pi}})^{1/\mathrm{Pi}}$. Thus, Ababou (1990), Ababou et al. (1994) proposed a power average expression for the principal components of the effective conductivity tensor $K_{ij,\mathrm{EFF}}$ in an N-dimensional medium, where the N exponents (powers Pi) were expressed in terms of N correlation scales (λi). Other authors investigated various semi-empirical formulae for power average upscaling (Journel et al. 1986; Deutsch 1989; Le Loc'h 1988; Dimitrakopoulos and Desbarats 1997; Desbarats 1992). Finally, let us mention some other approximate upscaling methods which are usually implemented numerically, but can also be viewed as quasi-analytical methods. Thus, Renard et al. (2000) proposed and implemented a heuristic method to calculate the equivalent conductivity based on the renormalization method. Their method is based on a combination of the bounds of Cardwell and Parsons. The resulting equivalent conductivity takes into account the three-dimensional geometric anisotropy of the medium, and yields a diagonal equivalent conductivity tensor (the principal directions of anisotropy are not computed, which is a limitation of the method).

The superposition method of Snow (1969), Kiraly (1969) and Oda (1985, 1986), yields equivalent conductivity of a fractured rock assuming impervious porous matrix. The method can be considered as another type of "fast" quasi-analytical upscaling method. The superposition method is exact only in special cases, such as parallel fracture networks. It has been extended to three-dimensional porous media with planar fractures and with non-negligible matrix permeability (Cañamón 2006; Ababou et al. 2011). For more details on this topic, see paragraph around Eq. (5) and the end of Sect. 2.2, where the superposition method is further discussed and compared with previous approaches. This paper will be essentially based on this type of method and several improvements and extensions will be provided.

In summary, some theoretical and approximate results from the literature on the upscaled conductivity of a heterogeneous medium have been presented. The review included analytical bounds and analytical expressions for effective conductivity in specific cases. Approximate methods have been also presented for numerically evaluating the equivalent conductivity of a finite sample numerically, but without solving the detailed flow problem in the heterogeneous porous sample (renormalization-type methods; superposition-type methods). These results can be applied not only to porous medium flow (hydraulic conductivity), but also to various other physical phenomena such as electrical conduction and heat diffusion.

In this paper, our focus is on fractured rock. The need for upscaling is motivated by modeling issues concerning geothermal exploitation, where coupled flow and heat transport occur in the porous rock matrix and also in many rock fractures that cannot

all be represented in detail. Upscaling the hydraulic conductivity leads to an equivalent continuum that is easier and less expensive to model numerically. This constitutes the main motivation of this paper. Now, given the available results and methods in the literature, it appears that the upscaling problem is particularly difficult for the case of fractured porous media, due mainly to the discontinuous nature and the large aspect ratio of the conductive fractures included in the porous matrix. To tackle this problem, this paper focuses on a "fast" superposition method which has already been used in various forms in the literature, and which can be viewed as quasi-analytical. Our aim in the remainder of this paper is to develop a more general type of "fast" upscaling method, which can treat correctly (accurately) the case of fractured porous media in three dimensions. This new method, to be developed here, is basically a modification of the three-dimensional flux superposition method of Ababou, Cañamon et al. (2011), itself based on the original superposition method of Snow 1969 and others. The goal of this paper is to explain the novel superposition method and to demonstrate its validity and limitations.

The remainder of the paper is, therefore, organized as follows. In Sect. 2, the proposed "fast" superposition method will be explained in detail. Sect. 3 describes how to obtain numerically the equivalent conductivity by direct flow simulations (this numerical $\underline{\underline{K}}_{\mathrm{EQ}}$ will serve as a reference to test the validity of the "fast" upscaling method). The validation will be presented in Sect. 4 for different types of fracture networks: "infinite size" fractures (defined further below) (Sect. 4.1); finite size fractures (Sect. 4.2); and finally, the more general case where both "infinite" and finite size fractures are present in the domain (Sect. 4.3). The important parameters in these analyses are: the fracture diameters; the density and connectivity of the fracture set (via the notion of excluded volume); and the fracture/matrix conductivity contrast (K_F/K_M). Discussions and conclusions will be presented in Sect. 5.

2 The Semi-analytical Superposition Method

2.1 General Description of the Method

Snow (1969) and Kiraly (1969) independently proposed a formulation for the equivalent conductivity of a fractured rock, with "infinite size fractures"[4] embedded in an impermeable matrix. This basic approach was later reproduced or extended by several authors (Oda 1986; others). Thus, a general expression of the conductivity tensor K_{ij} for a two-dimensional medium traversed by infinite size fractures was developed, and the final result K_{ij} was shown to depend only on the specific area and volume fraction of each individual fracture (Ababou et al. 1994). Defining an ensemble of M subsets of planar fractures, each with hydraulic apertures, sizes, and geometric parameters

[4] *Infinite size fractures*. It is understood in this paper that the term "*infinite size fracture*" or "*infinite fracture*" refers to any planar fracture that entirely crosses the upscaling domain. More precisely, if the upscaling domain is a convex region of finite volume (e.g., a three-dimensional parallelepiped), then an "infinite fracture" is a planar object that completely crosses the domain: it separates the domain in two subdomains, and its trace on the domain boundary is a closed curve. If the upscaling domain is infinite, then an "infinite fracture" is simply a planar fracture of infinite diameter.

(orientation angles of the normal to the fracture plane), they obtained the equivalent conductivity tensor of an arbitrary set of infinite-length fractures where each subset (labeled "m") is composed of N_m parallel fractures. The equivalent tensor is expressed as

$$K_{ij} = \frac{1}{12}\frac{g}{\nu}\sum_{m=1}^{M}\frac{A_m^3}{L_m}\left[\delta_{ij} - n_{i,m}n_{j,m}\right], \tag{5}$$

where A_m is the mean aperture of the parallel fracture subset "m"; L_m is the mean interspacing between fractures in parallel subset "m"; (δ_{ij}) is the Kronecker symbol; ($n_{i,m}$) is the ith component of the unit vector normal to fracture subset "m"; "g" is the acceleration of gravity ($g = 9.8$ m/s^2); "ν" is kinematic viscosity [m^2/s]. It should be mentioned that the number N_m of fractures within each parallel subset "m" does not appear in the above expression because averaging within each parallel subset has already been performed, resulting in the mean aperture "A_m" and mean spacing "L_m" of parallel set "m". This expression (Eq. 5) was later generalized to an arbitrary set of planar fractures of finite diameters and arbitrary orientations in three-dimensional space, taking also into account a permeable rather than impervious porous matrix (Ababou et al. 2011). The present paper is a further extension to better take into account the possible lack of connectivity of the set of finite diameter fractures (percolation effects).

In the present paper, each fracture is assumed a priori to have an anisotropic hydraulic conductivity, which is expressed in the local coordinate frame of the fracture as follows

$$\underline{\underline{K_{\mathrm{F}}}} = \begin{pmatrix} K_{\mathrm{F}}^{||} & 0 & 0 \\ 0 & K_{\mathrm{F}}^{||} & 0 \\ 0 & 0 & K_{\mathrm{F}}^{\perp} \end{pmatrix}, \tag{6}$$

where $K_{\mathrm{F}}^{||}$ and $K_{\mathrm{F}}^{\perp}$ are, respectively, the parallel and orthogonal components of the fracture conductivity tensor. These principal components could be obtained, in principle, from direct measurements. Alternatively, the parallel fracture conductivity $K_{\mathrm{F}}^{||}$ can be obtained theoretically by invoking the classical cubic law for flow between two parallel plates (planar Poiseuille flow): in this approach, the fracture walls are viewed as smooth parallel plates, flow is laminar (low Reynolds number), and the fracture is opened (not filled with porous material). This approach yields a parallel fracture permeability $K_{\mathrm{F}}^{||}$ [m^2] proportional to the squared aperture, and therefore, a parallel fracture conductivity $K_{\mathrm{F}}^{||}$ [m/s] also proportional to the squared aperture. The parallel fracture transmissivity $T_{\mathrm{F}}^{||}$ [m^2/s] is then proportional to the cubic aperture, hence the name "cubic law", (Tsang 1984; Brown 1987), among others. Finally, the orthogonal conductivity component is interpreted as infinite in this case ($K_{\mathrm{F}}^{\perp} \to \infty$), based on the fact that viscous dissipation due to fluid/solid friction is null in the transverse direction orthogonal to the fracture plane (in the absence of filling material between the fracture walls). Another possible representation of fracture flow is that each frac-

ture behaves, hydraulically, like a Darcian porous material with isotropic conductivity labeled "K_F". In the remaining of the paper, it will be assumed that $K_{\mathrm{F}}^{||} = K_{\mathrm{F}}^{\perp} = K_F$ in the fracture conductivity tensor of Eq. (6). Therefore, K_F is now scalar. Usually, the porous medium in the fracture is coarser and more permeable than the surrounding rock matrix and, therefore, $K_F > K_M$. Finally, in all cases, it is assumed that the porous rock matrix surrounding the fractures behaves according to the isotropic version of Darcy's law (scalar hydraulic conductivity K_M).

In the present superposition approach, the three-dimensional fractured porous domain is considered as the upscaling domain or "homogenization" domain of volume V_{hom}. This domain contains N_f fractures (or pieces of fractures) embedded in the permeable porous matrix. The first step of the superposition approach consists in disjoint partitioning of the domain into N_f "single-fracture" blocks (also named "unit blocks"). Each unit block contains a single fracture surrounded by a portion of the permeable matrix (the unit block in the upper right part of Fig. 1). The volume of each unit block is then calculated as

$$V_{\mathrm{block},f} = \pi\, R_f^2\, b, \tag{7}$$

where R_f is the lateral size of the block "f", equal to the equivalent radius of the fracture (this is the radius of the planar disc with the same area as the portion of the planar fracture located inside the homogenization domain). The transverse size "b" is the same for all unit blocks, and it is calculated by imposing volume conservation for the homogenization domain, as follows (Eq. 8)

$$\sum_{f=1}^{f=N_f} V_{\mathrm{block},f} = \sum_{f=1}^{f=N_f} \pi\, R_f^2\, b = V_{\mathrm{hom}}, \tag{8}$$

where R_f is the equivalent radius of the fracture "f", and b is the thickness of unit block "f". Equation 8 is essentially a volume conservation law.

Based on this decomposition of the fractured domain into unit blocks, two volume fractions are defined and will serve later for the implementation of the superposition method towards conductivity upscaling. First, the volume fraction of each discrete fracture "f", with respect to its corresponding block is defined in Eq. (9). Then, the volume fraction of each unit block "f", with respect to the homogenization domain is introduced in Eq. (10). The two volume fractions are given by

$$\Phi_f = \frac{V_f}{V_{\mathrm{block},f}} = \frac{\pi\, R_f^2\, a_f}{\pi\, R_f^2\, b} = \frac{a_f}{b}, \tag{9}$$

$$\Phi_{\mathrm{bloc},f} = \frac{V_{\mathrm{block},f}}{V_{\mathrm{hom}}}, \tag{10}$$

where a_f is the aperture of fracture "f".

The direction of the normal vector "$\underline{n}$" is represented, for each fracture "f", by a rotation matrix $\underline{\underline{Rot}}_f$. This matrix converts the coordinates of the local coordinate

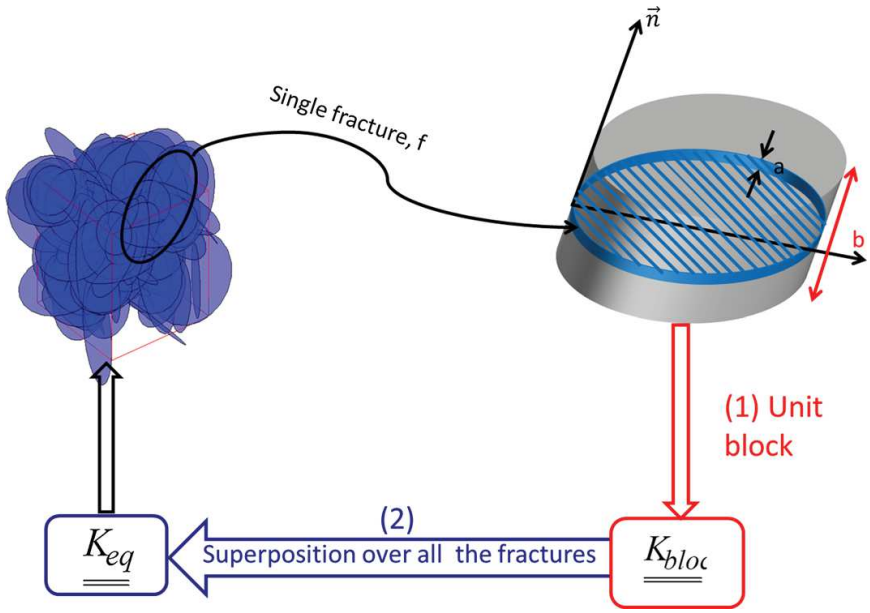

Fig. 1 Illustration of the superposition method for upscaling the hydraulic conductivity in two major steps: (1) upscaling over the single-fracture block, and (2) superposition over all unit blocks

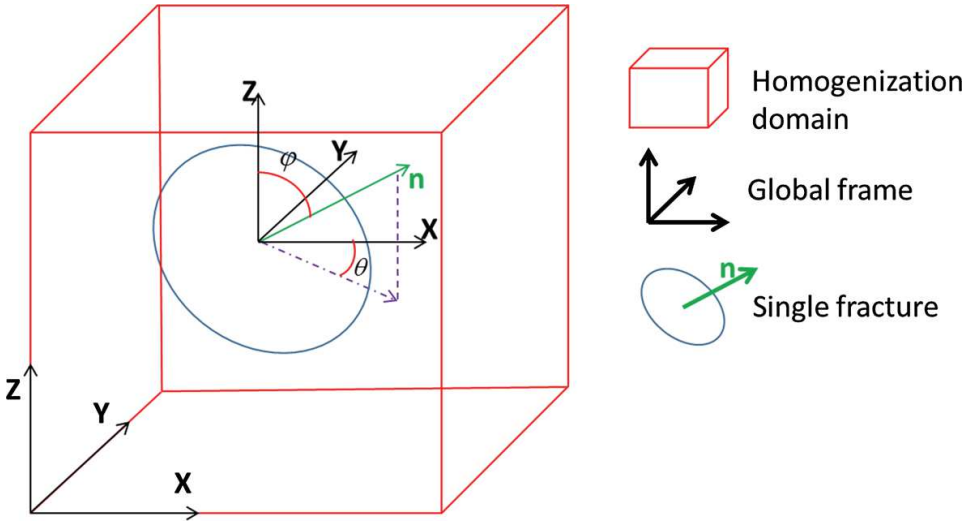

Fig. 2 Representation of the two spherical angles (polar angle φ and the azimuthal angle θ) defining the orientation of the unit vector "$\underline{n}$" (normal to a given planar fracture) with respect to the global frame of the homogenization domain. Here the domain is parallelepipedic, and a single fracture is shown for clarity

frame (fracture *"f"*) to those of the global coordinate frame (homogenization domain). The rotation matrix is given by

$$\underline{\underline{\mathrm{Rot}_f}} = \begin{pmatrix} \cos\theta\ \cos\phi & \sin\theta & -\cos\theta\ \sin\phi \\ -\sin\theta\ \cos\phi & \cos\theta & \sin\theta\ \sin\phi \\ \sin\phi & 0 & \cos\phi \end{pmatrix}, \tag{11}$$

where θ and φ are the spherical angles defining the orientation of the unit vector "$\underline{n}$" normal to the fracture plane. The two angles are illustrated in Fig. 2 for a single planar disc fracture.

2.2 Implementation Steps of the Quasi-Analytical Superposition Method

After the domain decomposition step (leading to a discrete number of "unit blocks"), hydraulic upscaling is implemented in two major steps, as illustrated in Fig. 1. In step (1), a first upscaling is performed at the scale of each single-fracture block and then in step (2), a second upscaling is implemented by superposing the fluxes over all unit blocks.

2.2.1 Step1: The Equivalent Conductivity of a Single-Fracture Block (First Upscaling)

First, a preliminary upscaling is performed on each "single-fracture" block, viewed as a composite medium comprising three "layers" (two matrix layers and one fracture layer). An analytical solution was obtained for flow through this sample by setting appropriate boundary conditions (piecewise linear pressure), calculating the volume averages of the resulting pressure gradient and flux vector fields, and finally, expressing the "exact" equivalent hydraulic conductivity of each "unit" block ($\underline{\underline{K}}_{\text{bloc}}$). The details are shown in Cañamon (2006) and in Ababou et al. (2011). The final result is

$$\underline{\underline{K}}_{\text{bloc}} = \begin{pmatrix} K_A & 0 & 0 \\ 0 & K_A & 0 \\ 0 & 0 & K_H \end{pmatrix}, \tag{12}$$

where K_A and K_H are the weighted arithmetic and harmonic means of K over the block and are given by

$$\begin{cases} K_A = (1-\Phi_f).K_M + \Phi_f.K_F^{\parallel} \\ K_H = \dfrac{1}{\frac{(1-\Phi_f)}{K_M} + \frac{\Phi_f}{K_{F^{\perp}}}} \end{cases}. \tag{13}$$

At this stage, each "single-fracture block" (unit block) is viewed as a new "fictitious" fracture with conductivity $\underline{\underline{K}}_{\text{bloc}}$. Note also that $\underline{\underline{K}}_{\text{bloc}}$ is a tensorial conductivity and is expressed in the local coordinate frame of the fracture. The conductivity tensor $\underline{\underline{K}}_{\text{bloc}}$ can then be expressed more generally in the global coordinate frame, using the rotation matrix $\underline{\underline{\text{Rot}}}_f$ (Eq. 11).

2.2.2 Step2: Superposition of Fluxes Over All Unit Blocks (Second Upscaling)

Having calculated the equivalent tensorial conductivity of each unit block, the flux contribution of each block is calculated under a given fixed pressure gradient. The flux contributions of all unit blocks are then superposed to obtain the total flux through the domain. This superposition takes into account orientations, diameters, and apertures of all fractures. It finally leads to a linear Darcy-type relation between flux and pressure gradient, with a tensorial equivalent conductivity ($\underline{\underline{K}}_{\text{EQ}}$), at the scale of the

homogenization domain. The resulting equivalent hydraulic conductivity takes the form

$$\underline{\underline{K_{\mathrm{EQ}}}} = \left\{ \sum_f \Phi_{\mathrm{bloc},f} \; \underline{\underline{\mathrm{Rot}_f}} \; \underline{\underline{K_{\mathrm{bloc},f}}} \; \underline{\underline{\mathrm{Rot}_f^t}} \right\}, \tag{14}$$

where $\underline{\underline{K}}_{\mathrm{EQ}}$ is the equivalent conductivity tensor of the porous fractured domain ("homogenization" domain); $\phi_{\mathrm{bloc},f}$ is the volumetric fraction of each unit block "f" and $\underline{\underline{K}}_{\mathrm{bloc},f}$ is the equivalent conductivity tensor of unit block "f" (expressed in the local coordinate frame of the block).

The expression given by Eq. (14) is an improved variant of the previous one proposed by Ababou et al. (2011). It takes into account, more directly, the volumetric fractions of fractures. Furthermore, it greatly simplifies the algorithm in the implementation of the method. Note that the resulting tensorial "$\underline{\underline{K}}_{\mathrm{EQ}}$" takes into account the geometric anisotropy of the fracture set, and at the same time, incorporates the permeability (K_M) of the porous matrix. The fact that the hydraulic conductivity of the matrix is taken into account here is an important point because in real geologic formations, the rock matrix may contain finer fractures that are not seen explicitly, and hence, matrix permeability should not be neglected. The connectivity structure of the fracture set is not directly taken into account by the above superposition approach (Eq. 14). This is true as well for earlier types of superposition methods (except for a tentative corrective factor proposed by Oda 1986). The present paper proposes (further below) an empirical method with corrective factors to take into account the effect of fracture set connectivity on the equivalent hydraulic conductivity of the fractured rock (Sects. 4.2 and 4.3).

3 Numerical Upscaling (Direct Simulations and Averaging)

To validate and test the superposition method, computational experiments have been developed in order to determine numerically (rather than theoretically) the equivalent hydraulic conductivity $\underline{\underline{K}}_{\mathrm{EQ}}$ of synthetic samples of three-dimensional fractured porous rocks. To determine numerically a macroscale equivalent hydraulic conductivity $\underline{\underline{K}}_{\mathrm{EQ}}$ for a heterogeneous medium (fractured porous medium), it is necessary to perform detailed numerical simulations of flow inside the porous matrix and the fractures (Sect. 3.1). In this work, the numerical simulations have been carried out in the steady state regime. Several simulations (at least three) are necessary for each fractured sample. Based on the detailed flow field obtained from the numerical experiments, an equivalence criterion (essentially some form of averaging) has been applied to determine numerically the equivalent hydraulic conductivity tensor $\underline{\underline{K}}_{\mathrm{EQ}}$ (Sect. 3.2). The choice of suitable conditions to be imposed at the boundaries of the three-dimensional domain is also important: this is discussed and analyzed in Sect. 3.3.

The subject of numerical upscaling in heterogeneous and fractured porous media has been an intensive area of research in recent decades. Numerical upscaling has been widely used to calculate block conductivities in hydrogeology and petroleum engineer-

ing. Earlier works on this topic include Warren and Price (1961) and Bouwer (1969), among others. Studies on numerical upscaling for heterogeneous and fractured media can be found in Wen and Gomez-Hernandez (1996), Renard and De Marsily (1997), Farmer (2002), Pouya and Fouché (2009), Ababou and Renard (2011) and Lang et al. (2014), among others. In particular, several approaches have been proposed in the literature regarding two essential aspects of numerical upscaling: (i) The equivalence criterion; and (ii) The boundary conditions (or other forcing conditions such as pumping). As will be seen below, our chosen equivalence criterion for numerical upscaling is essentially based on volume averaged flux and head gradient (Sect. 3.2). Furthermore, several possible types of boundary conditions for the numerical flow experiments will be discussed in detail (Sect. 3.3).

3.1 Direct Numerical Simulations of Darcy Flow

In this section, the numerical modeling (then numerical upscaling) of steady state flow in a saturated fractured porous medium is considered. Darcy's law is assumed to be valid inside the porous matrix (with hydraulic conductivity K_M), as well as inside the fractures (with hydraulic conductivity K_F). The areal flux density vector V [$m^3/s/m^2$] (also called Darcy velocity) is governed by Darcy's law. Combining it with mass conservation for steady flow, leads to the system of flow equations to be solved numerically

$$\begin{cases} \vec{\nabla} \bullet \vec{V} = 0 \\ \vec{V} = -K_M \vec{\nabla} H \quad \text{in } \Omega_M \\ \vec{V} = -K_F \vec{\nabla} H \quad \text{in } \Omega_F \end{cases}, \tag{15}$$

where Ω_M, Ω_F are, respectively, the porous matrix and the fractured domain, V is the Darcy velocity and H is the total hydraulic head (also known as piezometric head).

To solve this system of Darcy flow equations, two different tools have been used: the commercial software Comsol Multiphysics (Finite Elements), and the free software BIGFLOW3D (Finite Volumes). In BIGFLOW3D (Ababou et al. Ababou and Bagtzoglou 1993), the flux density vector (V) is inserted in the flux divergence equation, $\mathrm{div}(V) = 0$, and the resulting elliptic equation is solved for the hydraulic head H. The flux vector field V is then retrieved numerically from Darcy's head gradient law. The two tools present two complementary advantages: Comsol Multiphysics can handle adaptive meshing, which is very useful if high resolution is needed locally (e.g., at fracture intersections), and BIGFLOW code can handle much larger grids, with millions of cells or more, but without adaptive meshing. The choice of these two numerical software packages allows one to benefit from the short computation time (BIGFLOW3D) on the one hand, and customized adaptive meshing available in Comsol Multiphysics on the other hand. The use of each code will be indicated case by case in the sequel. For example, Fig. 3 displays graphically some computational IO's (Inputs and Outputs). The fractured porous medium is projected onto a three-dimensional cartesian grid of voxels (as shown at left). The iso-surfaces of hydraulic head H obtained by solving the flow equations (Eq. 15) are shown at right. In this example there are $N = 125$

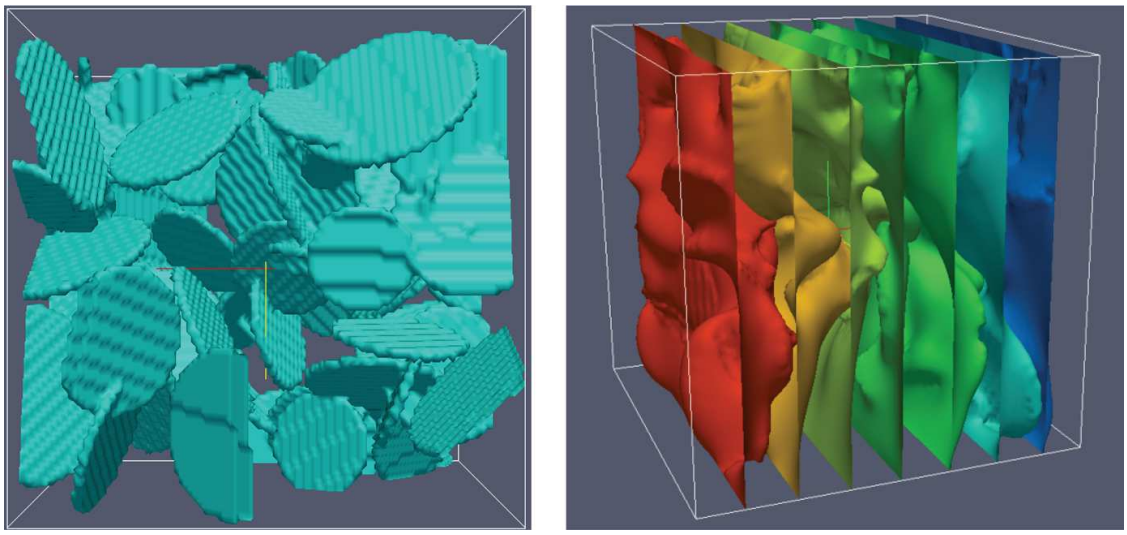

Fig. 3 Left: structured 3D Finite Volume Mesh (FVM) display of the fractured porous domain, with $N = 125$ planar disc fractures, and Ncells $\approx N1 \times N2 \times N3 \approx 106$ cells. Right: numerical flow simulation using the Finite Volume BIGFLOW 3D code (iso-surfaces of hydraulic head are shown)

planar disc fractures in the domain, and the fracture/matrix conductivity contrast is one million ($K_F/K_M = 10^6$). The three-dimensional domain was discretized into one million finite volume cells ($N_{\text{cells}} \approx N_1 \times N_2 \times N_3 \approx 10^6$).

A toolbox has been developed (in Matlab®) for numerically upscaling the hydraulic conductivity of the porous fractured medium based on the numerical flow field (H, V). For this purpose, the numerical tools mentioned above (FEM in Comsol, Finite Volumes in BIGFLOW3D) are used to solve the flow PDEs for each three-dimensional heterogeneous porous sample. These tools are combined with a "Live-Link" with Matlab in order to facilitate the numerical upscaling procedure (computing flux averages, etc.).

3.2 Averaging and Equivalence Criteria (Equivalent Darcy Law)

At the macroscale (homogenization scale), it is assumed here (by choice) that there exists an equivalent Darcy's law relating the volume average flux to the volume average gradient. This equivalence criterion is called VAF (volume average flux). As a consequence, at the homogenization scale, the laws governing the flow are

$$\left\{ \begin{array}{l} \nabla \cdot \left\langle \vec{V} \right\rangle = 0 \\ \vec{V} = -\underline{\underline{K_{\text{eq}}}} \left\langle \vec{\nabla} H \right\rangle \end{array} \right. , \tag{16}$$

where

$$\left\{ \begin{array}{l} \left\langle \vec{V} \right\rangle = \frac{1}{V_{\text{hom}}} \int_{V_{\text{hom}}} \vec{V} \, dV_{\text{hom}} \\ \left\langle \vec{\nabla} H \right\rangle = \frac{1}{V_{\text{hom}}} \int_{V_{\text{hom}}} \left(\vec{\nabla} H \right) dV_{\text{hom}} \end{array} \right. . \tag{17}$$

The angular brackets <•> in Eqs. (16, 17) indicate the volumetric average of the quantity "•". The "VAF" approach is widely used in the literature Pouya and Fouché (2009), Renard and Ababou (2009), Ababou and Renard (2011) and Lang et al. (2014) and others. It is worth mentioning here that other types of averaging have also been defined and used in the literature, such as "NSF" for net surface flux, among others. In addition, other criteria can be invoked, such as upscaling the mechanical work (or viscous dissipation work) rather than the flux (Ababou and Renard 2011).

A fully three-dimensional $\underline{\underline{K}}_{\mathrm{EQ}}$ tensor must be identified. Since each numerical simulation yields three scalar equations, the nine components of the $\underline{\underline{K}}_{\mathrm{EQ}}$ tensor ($i =$ 1,2,3 and $j = 1,2,3$) can be determined with three numerical simulations corresponding to three different directions of the imposed head gradient. Therefore, in each of the three numerical experiments ($m = 1, 2, 3$), it is assumed that

$$V_i^{(m)} = \left\langle \frac{\partial H^{(m)}}{\partial X_j} \right\rangle K_{\mathrm{EQ}ij} \; (m = 1, 2, 3) \,, \tag{18.a}$$

where implicit summation have been used on repeated indices. Finally, the following 9×9 linear system (Eq. 18.b) is obtained, which allows the determination of the nine components of the equivalent $\underline{\underline{K}}_{\mathrm{EQ}}$ tensor (presumed to be non-symmetric a priori) as follows

$$\begin{bmatrix}
\langle \nabla H_X^1 \rangle & \langle \nabla H_Y^1 \rangle & \langle \nabla H_z^1 \rangle & 0 & 0 & 0 & 0 & 0 & 0 \\
0 & 0 & 0 & \langle \nabla H_X^1 \rangle & \langle \nabla H_Y^1 \rangle & \langle \nabla H_z^1 \rangle & 0 & 0 & 0 \\
0 & 0 & 0 & 0 & 0 & 0 & \langle \nabla H_X^1 \rangle & \langle \nabla H_Y^1 \rangle & \langle \nabla H_z^1 \rangle \\
\langle \nabla H_X^2 \rangle & \langle \nabla H_Y^2 \rangle & \langle \nabla H_z^2 \rangle & 0 & 0 & 0 & 0 & 0 & 0 \\
0 & 0 & 0 & \langle \nabla H_X^1 \rangle & \langle \nabla H_Y^2 \rangle & \langle \nabla H_z^2 \rangle & 0 & 0 & 0 \\
0 & 0 & 0 & 0 & 0 & 0 & \langle \nabla H_X^2 \rangle & \langle \nabla H_Y^2 \rangle & \langle \nabla H_z^2 \rangle \\
\langle \nabla H_X^3 \rangle & \langle \nabla H_Y^3 \rangle & \langle \nabla H_z^3 \rangle & 0 & 0 & 0 & 0 & 0 & 0 \\
0 & 0 & 0 & \langle \nabla H_X^3 \rangle & \langle \nabla H_Y^3 \rangle & \langle \nabla H_z^3 \rangle & 0 & 0 & 0 \\
0 & 0 & 0 & 0 & 0 & 0 & \langle \nabla H_X^3 \rangle & \langle \nabla H_Y^3 \rangle & \langle \nabla H_z^3 \rangle
\end{bmatrix}
\begin{bmatrix} K_{11} \\ K_{12} \\ K_{13} \\ K_{21} \\ K_{22} \\ K_{23} \\ K_{31} \\ K_{32} \\ K_{33} \end{bmatrix}
=
\begin{bmatrix} \langle V_x^1 \rangle \\ \langle V_y^1 \rangle \\ \langle V_z^1 \rangle \\ \langle V_x^2 \rangle \\ \langle V_y^2 \rangle \\ \langle V_z^2 \rangle \\ \langle V_x^3 \rangle \\ \langle V_y^3 \rangle \\ \langle V_z^3 \rangle \end{bmatrix} . \tag{18.b}$$

This 9×9 linear system is easily solved numerically for the nine unknown conductivity components, given the flow data from the three numerical simulations. The flow data in this system are: the mean velocity components (right hand side vector 9×1) and the mean head gradient components (9×9 matrix). The previous linear system (Eq. 18.a–b) is solved, initially, for the non-symmetric $\underline{\underline{K}}_{\mathrm{EQ}}$ tensor, and then a symmetric tensor is obtained by taking the symmetric part ($(\underline{\underline{K}}_{\mathrm{EQ}+} \underline{\underline{K}}_{\mathrm{EQ}}^{\mathrm{T}})/2$). In most cases presented in this paper, the anti-symmetric part was negligible.

3.3 Boundary Conditions (BC) at the Homogenization Scale (Macroscale)

To solve the upscaled equations of flow at the macroscale, the boundary conditions have to be specified. There are various possible types of boundary conditions studied here: (i) permeameter conditions; (ii) linearly distributed head (constant gradient boundary conditions); and (iii) constant head conditions. (Note: in this subsection, the simulation results were obtained with Comsol Multiphysics).

3.3.1 Permeameter Boundary Conditions (PBC)

These conditions consist in imposing fixed heads on two opposite boundaries of the three-dimensional domain (H_0 and H_1) and setting the remaining boundaries to be impermeable (i.e., zero normal flux). These boundary conditions are simple and practical (for numerical, as well as physical laboratory experiments), especially if the purpose is only to determine the equivalent isotropic or diagonal hydraulic conductivity tensor in the frame of the sample. However, more generally, Kfoury et al. (2006) applied permeameter conditions to determine the full tensorial permeability on a two-dimensional sample, and later on, Li et al. (2011) determined the full three-dimensional tensor with the same permeametric conditions. The full tensor determination from these boundary conditions (PBC) requires more complicated averaging procedures: cross-differentiation (Kfoury et al. 2006); skin technique (Li et al. 2011). In this study, the purpose is determining the full equivalent tensor for a given averaging criterion "VAF" under various types of boundary conditions. The permeametric boundary conditions (PBC) will be used only in Sect. 4.2.1 to compare the sensitivity of percolation phenomena to the type of boundary conditions.

3.3.2 Immersion Boundary Conditions (IBC)

"Immersion" boundary conditions (IBC) are implemented by imposing a linearly distributed head $H(x,y,z)$ on the boundary of the sample (that is, on all six faces of the boundary, if the sample is parallelepipedic). These boundary conditions are called "immersion" boundary conditions, because the sample appears to be "immersed" in an infinite domain with a "far field" hydraulic gradient imposed everywhere outside the rock sample. The resulting boundary condition (IBC) can be expressed as a linear head profile ($H\left(\overrightarrow{x}\right) = H_0 - \overrightarrow{J_0} \bullet \overrightarrow{x}$), where H_0 is the hydraulic head at the origin, and $\overrightarrow{J_0}$ is a spatially imposed constant hydraulic gradient.

In the literature, the linear head or linear pressure boundary condition has been widely used for studying PDE problems of the form $\mathrm{div}(K\ \mathrm{grad}\ u) = f$ for constant and variable K. Earlier mathematical references include Bamberger (1977). This type of boundary condition has also been used by Long et al. (1982), and more recently by Pouya and Fouché (2009), Ababou and Renard (2011), and others, for theoretical and numerical upscaling of permeability in heterogeneous and/or fractured media. The IBC flow condition seems to be consistent with the physics of flow in natural rocks: the homogenized sample (sub-domain) is not isolated from the rest of the flow domain, and it is affected by the far field head gradient of the surroundings. By the same token, the IBC gives a large degree of freedom to flow: for instance, under steady flow, water can circulate between any two boundary faces of the three-dimensional domain, and it can also flow out at one point and re-enter at another point of the same boundary face. Indeed, there may exist a flow re-entry at the intersection of one isolated finite size fracture with the domain boundary (Fig. 4). Such boundary re-entry effects, caused by "IBC", can be quite significant, as can be seen in Fig. 4 (zoom insert): the small isolated fracture intersecting a boundary face participates significantly to the volumetric average of velocity, even though the fracture is not

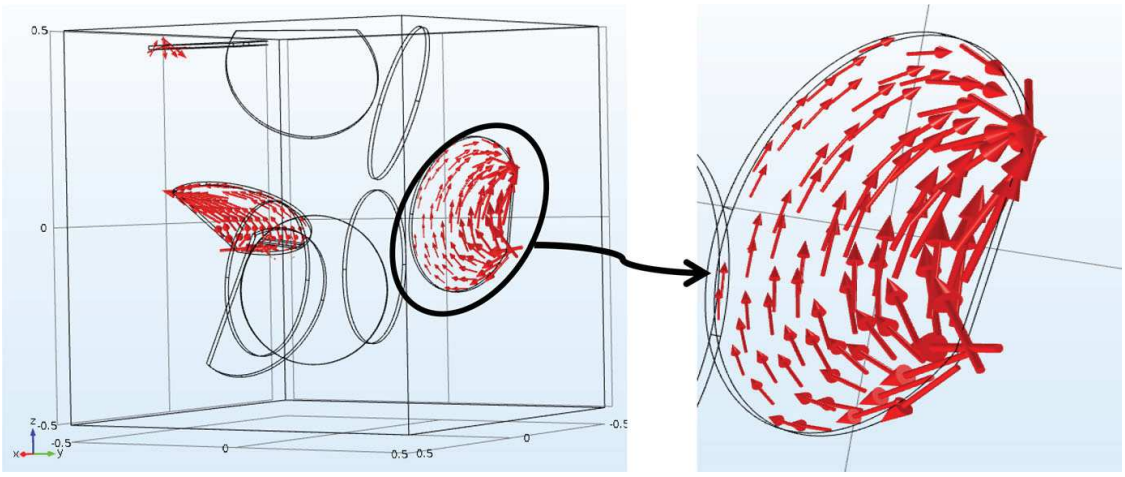

Fig. 4 Left: representation of the Darcy velocity field (arrows) in the case of "IBC". There are nine fractures of radius $R = 2\ [m]$. Domain size is $10 \times 10 \times 10\ \mathrm{m}^3$. Conductivity contrast is $K_F/K_M = 10^6$. Right: zoom on an isolated fracture intersecting one boundary face, illustrating the re-entry effects

connected to any percolating cluster inside the domain. The consequences will be examined in Sect. 3.4, where it will be concluded that other boundary conditions are more suitable for studying percolation effects.

3.3.3 Constant Heads Boundary Condition (CHBC)

The previously described immersion boundary conditions (labeled "IBC") could be replaced by other boundary conditions in order to avoid the effects of flow re-entry at boundary/fracture intersections (described above), while still allowing the full determination of an equivalent conductivity tensor $\underline{\underline{K}}_{\mathrm{EQ}}$. One such method consists in imposing constant heads, rather than linearly distributed heads, on all boundary faces: H_0 and H_1 are imposed on two opposite boundary faces, and $(H_0 + H_1)/2$ is imposed on all the other "lateral" boundary faces. For this reason, this method is labelled "constant heads boundary conditions" (CHBC). This choice of boundary conditions comes at a price: the discontinuity of boundary heads at corners and edges. However, the comparison just below reveals the possible advantages of CHBC.

3.4 Comparison of Different Types of Boundary Conditions (IBC Versus CHBC)

This section presents a comparison of the numerical upscaling method based on two types of boundary conditions: "immersion boundary conditions (IBC)" and "constant heads boundary conditions (CHBC)". The comparisons are made for the case of a three-dimensional set of statistically isotropic, "infinite size" planar fractures (in practice these are generated as planar disc fractures with diameters much greater than domain size, as explained in footnote in Sect. 2.1). Matrix conductivity ($K_M = 10^{-5}$ m/s) is chosen much lower than fracture conductivity ($K_F = 10$ m/s), in order to emulate the case of a discrete fracture network (here the fracture/matrix conductivity ratio is very high: one million). The numerical $\underline{\underline{K}}_{\mathrm{EQ}}$ tensors obtained with IBC and CHBC are relatively close, but not identical, as shown in Fig. 5. Nevertheless, it can be

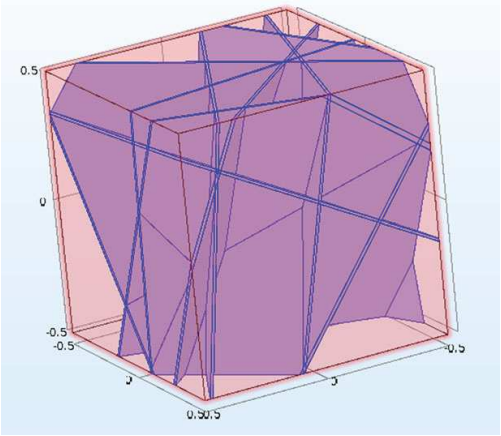

$$\begin{cases} \underline{\underline{K_{EQ}}}_{IBC} = \begin{pmatrix} 4.11 & & \\ & 4.29 & \\ & & 4.36 \end{pmatrix} \\ \underline{\underline{K_{EQ}}}_{CHBC} = \begin{pmatrix} 3.33 & & \\ & 3.43 & \\ & & 3.74 \end{pmatrix} \end{cases}$$

Fig. 5 Left: fracture network composed of "infinite" fractures (all factures completely intersect the homogenization domain). Right: equivalent hydraulic conductivity tensor $\underline{\underline{K}}_{\mathrm{EQ}}$ obtained for the two boundary conditions [immersion (IBC) and constant heads (CHBC)]

considered that the two results are similar, given the high contrast K_F/K_M, and given the discontinuity effects due to CHBC at corners and edges are weak in this case.

However, the conclusions are quite different for a case involving a non-percolating network of finite size fractures. The case considered here is a fracture set comprising nine planar disc fractures, such that the fractures do not traverse the domain boundaries individually and do not form a percolating cluster of fractures collectively (Fig. 6 on the left). The equivalent conductivity tensors $\underline{\underline{K}}_{\mathrm{EQ}}$ obtained numerically with the two different types of boundary conditions (IBC, CHBC) are very different, as shown in Fig. 6 (on the right). In this example, it can be clearly seen (because there are very few fractures in the domain) that there does not exist a percolating cluster of fractures. Therefore, one would expect the equivalent hydraulic conductivity $\underline{\underline{K}}_{\mathrm{EQ}}$ to be very close to the conductivity of the porous matrix (here $K_M = 10^{-5}$ m/s). As can be seen, the resulting $\underline{\underline{K}}_{\mathrm{EQ}}$ obtained with the constant Heads boundary conditions (CHBC) yields values much closer to those expected. The conductivity tensor from IBC overestimates the equivalent hydraulic conductivity by two orders of magnitude (~600). This overestimation due to IBC boundary conditions is explained by a flow re-entry phenomenon at the intersection of one isolated fracture with a boundary face (as in Fig. 4, zoom insert). For this reason, "constant heads boundary conditions (CHBC)" has been chosen for the numerical experiments to be presented in the remainder of this paper. The previous comparison justifies the choice of CHBC, particularly for poorly percolating fracture sets, even if these conditions could generate discontinuities at the borders (while IBC maintains continuity at the borders).

4 Comparisons, Validation Tests, and Extension of Upscaling Method

This section deals with comparison of the upscaled conductivity obtained with the "fast" superposition method developed earlier, with the one obtained numerically. The numerical simulation results are exploited for several different fracture network configurations (in terms of fracture size, density, connectivity, and fracture/matrix conductivity ratio). The objective is to validate the fast upscaling method (superposition

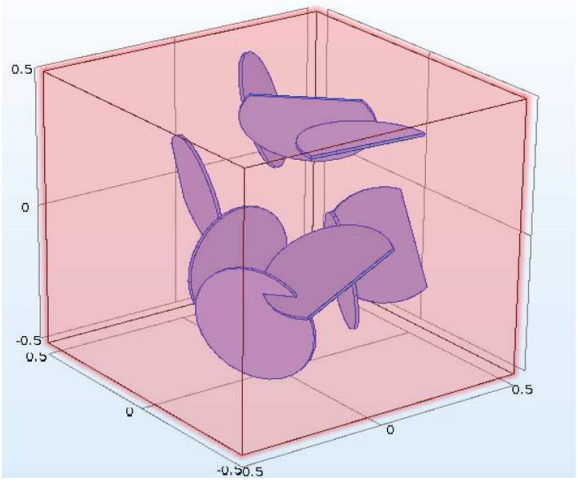

$$K_{IBC} = \begin{pmatrix} 0.009 & 0.001 & 0.0009 \\ 0.001 & 0.003 & 0.001 \\ 0.0009 & 0.001 & 0.006 \end{pmatrix}$$

$$K_{CHBC} = \begin{pmatrix} 1.2E^{-5} & 2E^{-7} & 2E^{-7} \\ 2E^{-7} & 1.7E^{-5} & 8E^{-7} \\ 2E^{-7} & 8E^{-7} & 1.3E^{-5} \end{pmatrix}$$

Fig. 6 Left: fracture network composed of finite size fractures. Right: equivalent hydraulic conductivity tensors $\underline{\underline{K}}_{EQ}$ obtained for the two boundary conditions, immersion (IBC) and constant heads (CHBC)

method), to improve it and propose possible extensions. Because the behavior of the equivalent hydraulic conductivity greatly depends on the size of fractures, the following types of fracture networks are treated separately: infinite size fractures (Sect. 4.1); then finite size fractures (Sect. 4.2); and finally a mixture of infinite and finite size fractures (Sect. 4.3). Most of the numerical tests are conducted for a large contrast of fracture/matrix conductivity.

4.1 Comparisons and Validation Tests: Case of Infinite Size Fractures

Several cases have been tested, involving two-dimensional and three-dimensional sets of infinite size fractures: parallel fractures; inclined set of parallel fractures; Cartesian network, which implies that the fracture orientations are aligned with spatial frame axes (X, Y and Z directions); random set of three-dimensional Poissonian fractures with statistically isotropic orientation among other cases. A fracture set is Poissonian if the fracture centers (X, Y, Z) are distributed according to a three-dimensional Poisson point process; the positions X, Y, Z are uniformly distributed (Vanmarcke 1983). A fracture set is statistically isotropic in the following sense: consider the intersection points of their unit normal vectors with the unit sphere; these points must be distributed uniformly on any spherical cap on the surface of the unit sphere.[5] Reminder: the term "infinite" indicates that each fracture has a diameter larger than the diameter of the rock sample domain (Sect. 2.1). In that case, each individual fracture is percolating "on its own", which means that each individual fracture connects at least two boundary faces. Obviously, the network is also fully percolating as well.

As expected, for fully connected and percolating fracture networks, the results obtained by numerical experiments show that upscaled permeability tensors $\underline{\underline{K}}_{EQ}$ obtained by the present fast superposition and by numerical experiments are in good

[5] The consequence in three-dimensional space is that the longitude angle Θ must be distributed uniformly in $[0, 2\pi]$, and (independently) the latitude angle φ has its cosine distributed uniformly in $[-1, +1]$.

Table 1 Detailed results of the comparison between numerical upscaling and superposition upscaling for the fracture set of Fig. 7 (parallel inclined fracture set)

Numerical upscaling	Upscaling by fast superposition method
$K_{\text{numerical}} = \begin{pmatrix} 0.00235 & 0 & 0.00312 \\ 0 & 0.0109 & 0 \\ 0.00312 & 0 & 0.009806 \end{pmatrix}$	$K_{\text{superposition}} = \begin{pmatrix} 0.00226 & 0 & 0.00576 \\ 0 & 0.01249 & 0 \\ 0.00576 & 0 & 0.01483 \end{pmatrix}$
Eigen values:	Eigen values:
$K^*_{\text{numerical}} = \begin{pmatrix} 0.00121 & 0 & 0 \\ 0 & 0.0109 & 0 \\ 0 & 0 & 0.0109 \end{pmatrix}$	$K^*_{\text{superposition}} = \begin{pmatrix} 0.0019 & 0 & 0 \\ 0 & 0.0124 & 0 \\ 0 & 0 & 0.0170 \end{pmatrix}$
Eigen vectors:	Eigen vectors:
$\begin{pmatrix} V_1 & V_2 & V_3 \\ 0.939 & 0 & 0.341 \\ 0 & -1 & 0 \\ -0.341 & 0 & 0.939 \end{pmatrix}$	$\begin{pmatrix} V_1 & V_2 & V_3 \\ 0.931 & 0 & 0.362 \\ 0 & -1 & 0 \\ -0.362 & 0 & 0.931 \end{pmatrix}$

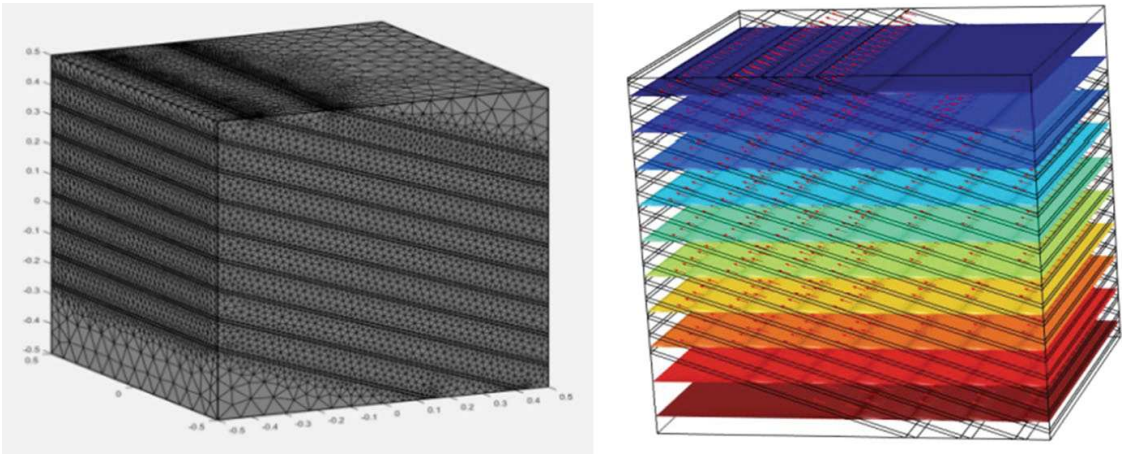

Fig. 7 Left: Finite element mesh of a fractured porous medium containing a set of inclined fractures. Right: results of a numerical flow simulation used for numerical upscaling for the same fracture set: iso-surfaces of piezometric heads and velocity vector arrows

agreement both in terms of norm and principal directions. As an example, it is shown in Table 1 the detailed results for a set of inclined fractures, depicted in Fig. 7, with $K_F = 0.1$ [m/s] and $K_M = 0.0001$ [m/s]). There is an excellent agreement between the superposition method and the numerical upscaling. The eigenvalues and eigenvectors of the equivalent conductivity tensor $\underline{\underline{K}}_{\text{EQ}}$ are also shown in the table, in order to verify that the superposition method is in agreement with the numerical upscaling for the full anisotropic conductivity tensor (The matrix $\underline{\underline{K}}_{\text{EQ}}$ is non-diagonal due to the inclined fractures).

Additionally, the results of numerical upscaling for different fracture densities have been analyzed. First, the equivalent $\underline{\underline{K}}_{\text{EQ}}$ tensor obtained either numerically or by superposition, is diagonalized. This serves several purposes: examining the eigenvalues and eigenvectors qualitatively, and also calculating the trace of the tensor. Because $\underline{\underline{K}}_{\text{EQ}}$ is symmetric definite positive, the trace of $\underline{\underline{K}}_{\text{EQ}}$ is equivalent to the Frobenius norm of the square root B of the matrix $\underline{\underline{K}}_{\text{EQ}}$ such that $\text{BB}^{\text{T}} = \underline{\underline{K}}_{\text{EQ}}$. More precisely, the square-root

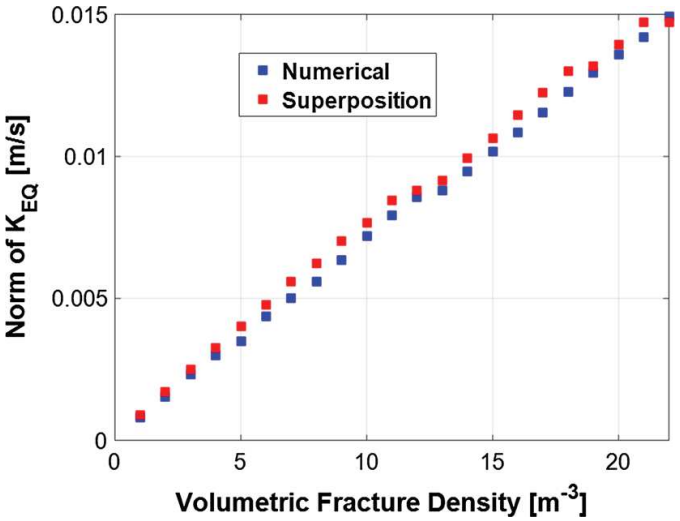

Fig. 8 Plot of the norm of equivalent hydraulic conductivity tensor, as a function of volumetric fracture density $\rho_{0,3}$ (blue symbols for the superposition method, red symbols for numerical upscaling)

matric B is given by $B = PD^{1/2}$ where P is the passage matrix containing column eigenvectors, and D is the diagonal eigenvalues matrix. Hereafter, the term "norm" of the conductivity tensors refers to the following expression

$$\|K\| = \left\| \begin{matrix} K^*_{xx} & 0 & 0 \\ 0 & K^*_{yy} & 0 \\ 0 & 0 & K^*_{zz} \end{matrix} \right\| = \frac{1}{3}(K^*_{xx} + K^*_{yy} + K^*_{zz}), \tag{19}$$

where the stars * refer to the principal components of $\underline{\underline{K}}_{\mathrm{EQ}}$.

Figure 8 shows the norm of the equivalent hydraulic conductivity tensor as function of the volumetric density of fractures $\rho_{0,3}$ [m^{-3}] for a three-dimensional Poissonian network with statistically isotropic orientation. The fractures in this figure are "infinite" (percolating fractures). The volumetric fracture density $\rho_{0,3}$ is defined as the number of fractures per unit volume ([number of fractures/m^3] or [m^{-3}]). As it can be seen in that plot, there is a good agreement between the equivalent hydraulic conductivities obtained by the superposition method and by numerical upscaling. A slight difference can be observed however, especially with high fracture densities, and it is generally attributed to numerical errors. The effect of the conductivity contrast (K_F/K_M) in the upscaling values has also been analyzed. Figure 9 shows the numerically upscaled and quasi-analytical (superposition) values of equivalent hydraulic conductivities for different fracture/matrix conductivity contrasts (from one to one million), for a three-dimensional Poissonian fracture network. The diameters in this case are larger than domain size ("infinite" fractures). Here, the density is $\rho_{0,3} = 20.0$ [m^{-3}].

Based on Fig. 9, it can be concluded that the superposition method yields a good estimation of the equivalent hydraulic conductivity of three-dimensional fracture networks with "infinite" fractures for different conductivity contrasts (K_F/K_M). This influence of the conductivity contrast can be important, because the matrix may contain finer fractures that are not seen explicitly, and hence, its permeability must not be neglected. These results confirm so far that the quasi-analytical superposition method is a correct method for upscaling "infinite" fractures regardless of their orientation

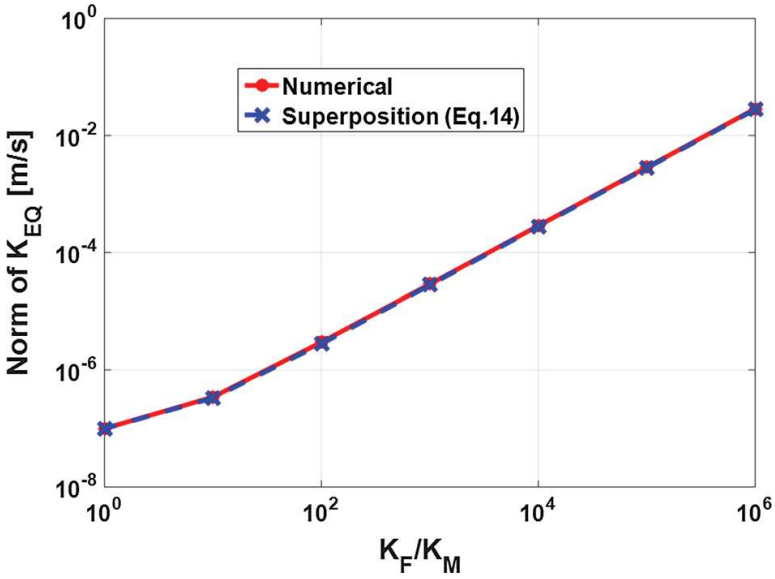

Fig. 9 Log-log plot of the norm of the equivalent hydraulic conductivity tensor as a function of the conductivity contrast (K_F/K_M) for the previous example

or aperture distributions, and without the need for detailed numerical solution of the matrix/fracture flow equations.

4.2 Extension to Finite Size Fractures

The aim of this section is to provide an expression based on the superposition method [i.e., an extension of Eq. (14)], in order to estimate the equivalent conductivity tensor for a large three-dimensional domain (the entire reservoir domain for example) containing only finite size "non-crossing fractures". The term "non-crossing fracture" refers to the case where the fracture diameter is not large enough (compared to the domain diameter) to connect two boundary faces of the parallelepipedic domain. However, depending also on fracture density, it is possible to obtain a percolating cluster formed by the intersection of several finite size "non-crossing" fractures. Generally, with finite size fractures, it is expected that connectivity effects are important for the equivalent hydraulic conductivity, and particularly when the fracture/matrix conductivity contrast (K_F/K_M) is high. In this subsection, the simulation results were obtained with the BIGFLOW code (unless indicated otherwise). Finally, it should be emphasized that only networks with Poissonian and isotropic spatial distributions are tested for the validation of the proposed extensions in this section and the next (Sect. 4.3).

4.2.1 Introduction to "Finite Size" Fracture Networks Characteristics (Critical Density and Percolation)

Our objective is to study connectivity effects by conducting numerical flow experiments in a finite fractured domain, with high conductivity contrast K_F/K_M. Under

these conditions, the hydraulically conductive medium is a network of "finite size"[6] planar disc fractures with negligible matrix permeability. In order to reduce border effects as much as possible, the fracture network has been preprocessed prior to flow experiments, by eliminating all the isolated fractures that intersect at least one edge or one corner of the three-dimensional parallelepipedic domain. This procedure eliminates any single isolated fracture connecting two or more boundary faces.

In this type of configuration (i.e., with a large computational domain containing only small size fractures), it is useful to consider a critical density $\rho_{EX,c}$ by analogy with percolation theory. This quasi-percolation density, or critical density, can be defined, in general, as the fracture density above which the first cluster of fractures connecting two different boundary faces of the domain is formed (initiation of percolation). However, this "critical density" takes here a somewhat different meaning. Mathematical percolation theory deals with infinite domains, while here the computational domain is of finite size. In addition, percolation theory deals essentially with two possible types of conducting networks (site networks, and bond networks), while this work deals with planar disc conductors embedded in a three-dimensional porous matrix. Sahimi (1995) gives a review of percolation theory. Conduction and percolation in fractured media have been studied in Sahimi (1995), Berkowitz and Adler (1998), Mourzenko et al. (2005) and Adler et al. (2012), and others. Finite size effects on percolation phenomena were studied, more recently, by Adler et al. (2012). To sum up, the above-mentioned critical percolation density ($\rho_{EX,c}$) can be a useful concept for extending the superposition method to finite size fracture networks. $\rho_{EX,C}$ will be defined more precisely below, and then it will be used it to take into account two different behaviors of the fractured medium, depending on fracture density. If the fracture density is less than the critical density, the fracture network is not percolating; it does not connect any two different boundary faces of the upscaling domain. If the fracture density is greater than the critical density, it exists one or several percolating clusters connecting two or more boundary faces of the upscaling domain. The use of this critical percolation density ($\rho_{EX,c}$) in the new formulation of the superposition method will be explained below in Sects 4.2.2 and 4.3. Let us focus here on the definition of the appropriate density "ρ_{EX}" via the notion of "excluded volume". The excluded volume is defined, in the general case, as the averaged volume around one object within which a second object must have its center in order for the two objects to intersect (Charlaix et al. 1984). First the "excluded volume" $V_{EX,f}$ of a given fracture "f" is defined. The total excluded volume V_{EX} is then the sum $\Sigma V_{EX,f}$ calculated over all fractures ($f = 1,2,\ldots,N$). Finally, the fracture density "$\rho_{EX,C}$" is obtained by dividing V_{EX} by the volume V_{hom} of the upscaling domain: $\rho_{EX} = V_{EX}/V_{hom}$.

Let us focus now on determining the excluded volume $V_{EX,f}$ of a single fracture "f". The definition of the excluded volume can be illustrated more easily, as shown in Fig. 10, for the case of a set of fracture segments in two-dimensional space. The equivalent of an excluded volume in three dimensions is the excluded area in two dimensions. Fracture diameters in three dimensions are replaced by fracture lengths "L" in two dimensions, and the two orientation angles (θ,φ) in three dimensions are

[6] A *"finite size" fracture* is any planar fracture which does not entirely cross the upscaling domain: the opposite of "infinite sire" fracture mentioned in Sect. 2.

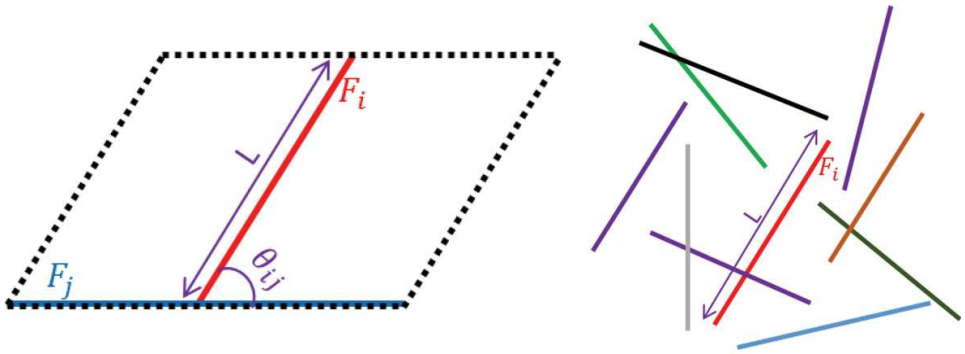

Fig. 10 **a** Representation of two arbitrary fracture segments and of their excluded area, delimited by the black dashed parallelogram (two-dimensional space). **b** Representation of a statistically isotropic network of fracture

replaced by the single angle (θ) in two dimensions. Figure 10a illustrates the calculation of the excluded area for a given fracture "F_i" with its given fracture length "L" and its given orientation θ_i. A second fracture segment F_j is selected, with its given length "L" and its given orientation θ_j. The relative orientation between the segments F_i and F_j is $\theta_{ij} = \theta_i - \theta_j$. The excluded area is obtained, as explained in Balberg et al. (1984), by translating the second segment F_j to all positions such that F_j intersect F_i (relative orientations are not changed). The resulting excluded area of the pair of fractures (F_i,F_j) is the area of the dotted parallelogram ($A_{EX} = L^2 \sin\theta_{ij}$) shown in Fig. 10a. A statistically isotropic network of fracture segments is now considered, with random angle θ uniformly distributed in [0, 2π] and deterministic length "L", as illustrated in Fig. 10b. The mean excluded area of this statistical network is calculated by averaging over all possible orientations θ_{ij} of the random fracture segments. The result, $A_{EX} = 2L^2/\pi$, was obtained by Balberg el al. (1984).

In three dimensions, Adler et al. (1999) studied the excluded volume of planar convex polygonal fractures,[7] each with a given area "A", a given perimeter "P", and orientation angles (Θ,Φ) defined by its normal. Let us consider two such fractures F_i and F_j, with their respective areas, perimeters, and angles. These two planar fractures have a relative angle "φ_{ij}" with respect to each other. Charlaix (1984) and Adler et al. (1999) obtained the excluded volume for two fractures of different sizes; in the special case where A and P are the same for the two fractures, the result is

$$V_{EX}(i, j) = \frac{2 \sin \varphi_{ij}}{\pi} A P. \tag{20.a}$$

For statistically isotropic networks in three dimensions, the average $<\sin \varphi_{ij}>$ is equal to $\pi/4$, and then, the mean excluded volume is

$$V_{EX} = \frac{1}{2} A P. \tag{20.b}$$

[7] The planar disc fractures studied in this work are a special limit form of planar convex polygons as the number of edges goes to infinity.

Finally, the last formula (Eq. 20.b) is used to calculate fracture by fracture the excluded volume, and then to deduce a dimensionless fracture density ρ_{EX} as follows

$$\begin{cases} V_{EX,f} = \frac{1}{2} A_f P_f \\ V_{EX} = \sum_f V_{EX,f} \\ \rho_{EX} = \frac{V_{EX}}{V_{hom}} \end{cases}, \tag{21}$$

where $\rho_{EX,C}$ is the dimensionless fracture density, V_{EX} and V_{hom} are respectively the total excluded volume of all the fractures, and the total volume of the homogenization domain (upscaling domain). It was demonstrated that for isotropic fracture networks, $\rho_{EX,C}$ is also equal to the mean number of intersections per fracture (Charlaix et al. 1984): this indicates the importance of $\rho_{EX,C}$ is a measure of the degree of connectivity of the fracture network. The critical excluded volume $V_{EX,C}$ is then defined as the excluded volume above which a percolating cluster appears. The corresponding critical percolation density $\rho_{EX,C}$ is finally computed as the critical excluded volume $V_{EX,C}$ divided by the total volume of the domain (Eq. 22)

$$\rho_{EX,C} = \frac{V_{EX,C}}{V_{hom}}. \tag{22}$$

It is important to highlight here that the latter expressions of ρ_{EX} (Eq. 21) and of $\rho_{EX,C}$ (Eq. 22) are the same as the ones used by Mourzenko et al. (2005) where they found that $\rho_{EX,C}$ was not very sensitive to fracture size in predicting percolation. Finally, this dimensionless density $\rho_{EX,C}$ was found to be only "slightly" sensitive to the orientation distribution of the network in predicting percolation (Mourzenkou et al. 2009). After the presentation of the critical density $\rho_{EX,C}$ and other related quantities, the next part will explain how this critical density $\rho_{EX,C}$ has been numerically determined (Sect. 4.2.1), and how it was used for a new extension of the superposition method that can account for the degree of connectivity of the fracture set (Sect. 4.2.2).

4.2.2 Determination of the Critical Density

The critical density in this work is defined statistically and determined numerically because there are no theoretically exact methods allowing its unique determination in a finite fractured domain (again, recall that this work is not dealing with infinite domain percolation theory). The numerical procedure to determine the critical percolation density consists in conducting a series of numerical flow experiments for a single replicate of the fracture porous medium with increasing fracture density (and a fixed high contrast K_F/K_M). The different densities are obtained by adding fractures from a pre-set of random fractures: $N = 1000$ disc fractures are first generated, the number of fractures are, therefore, increased by sampling into this pre-set of 1000 random fractures. This numerical procedure is equivalent to generating several independent realizations of fractures sets. For instance, in a sequence of 1000 generated fractures, the first subset of 100 fractures is independent from the 2nd subset (fractures N°101 to N°200). The equivalent hydraulic conductivity is then determined for each density by numerical upscaling from the computed flow using CHBC. The critical "percolation"

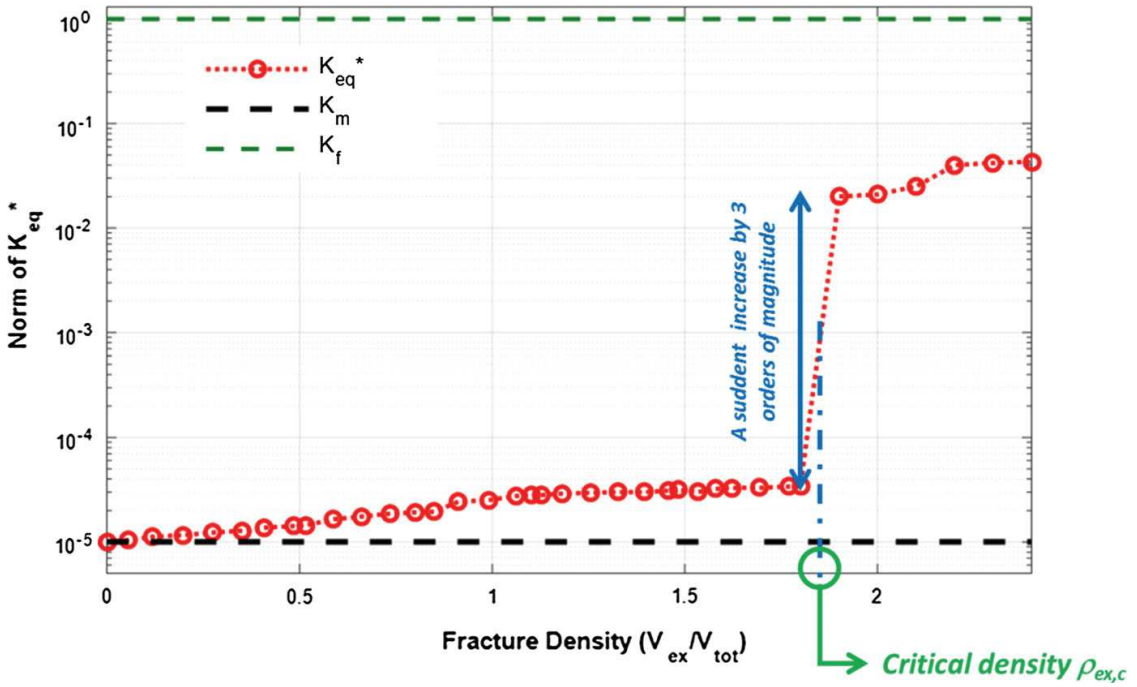

Fig. 11 Plot of $\underline{\underline{K}}_{EQ}$ (norm) as a function of fracture density (ρ_{EX}) for a single realization of a three-dimensional fracture network. A sudden jump of the norm of $\underline{\underline{K}}_{EQ}$ by 3 orders of magnitude is observed; the corresponding density to the jump is the critical density ($\rho_{EX,C}$)

density is detected by a sudden increase of the equivalent hydraulic conductivity with respect to density. The determination of $\rho_{EX,C}$ for a single realization of a three-dimensional fracture network is shown in Fig. 11.

To obtain values of $\rho_{EX,C}$ representative of the percolation behavior of three-dimensional fracture networks, multiple realizations of the network are generated, with constant fracture radius (non-random). For example, $N \times M = 30{,}000$ statistically independent planar disc fractures (isotropic Poissonian) are initially generated. Then, the $N \times M$ fractures are divided into $M = 30$ networks, each containing $N = 1000$ fractures. The previously described procedure to determine the critical density $\rho_{EX,C}$ is then applied to each of the 30 realizations. Finally, the "ensemble mean" critical density $E(\rho_{EX,C})$ is determined over the M realizations of the fracture network (Fig. 12). Note: from now on, the mean $E(\rho_{EX,C})$ will be denoted as "$\rho_{EX,C}$" for short.

As shown in Fig. 12, the mean critical density calculated by the previous procedure is $\rho_{EX,C} \approx 0.75$. However, Mourzenko et al. (2005) have shown that there exists a universal critical density, independent of fracture size: the critical density for disc fractures was found to be $\rho_{EX,C} = 2.31$. To understand this difference, other possible definitions of percolation can be considered. For example, a cluster is counted as "percolating" only if it relates two opposite boundary faces of the three-dimensional parallelepipedic domain. This definition corresponds physically to the application of PBC for the numerical determination of the equivalent hydraulic conductivity tensor. In that case (PBC), the obtained critical density values are found to be close to the value 2.31 obtained by Mourzenko et al. (2005). More specifically, a typical numerical simulation (with Comsol Multiphysics) with permeameter boundary conditions (PBC) is presented in Fig. 13, in which the permeable boundaries are only the top and bottom

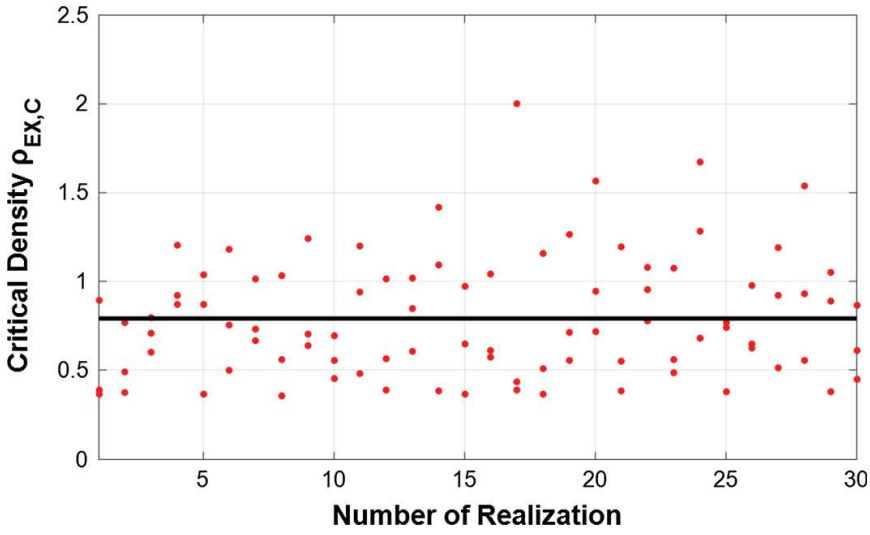

Fig. 12 Determination of the critical density of percolation ($\rho_{EX,C}$) over multiple realizations ($M = 30$). The ensemble mean value of $\rho_{EX,C}$ is retained as the final critical density of percolation. Here $\rho_{EX,C} \approx 0.75$

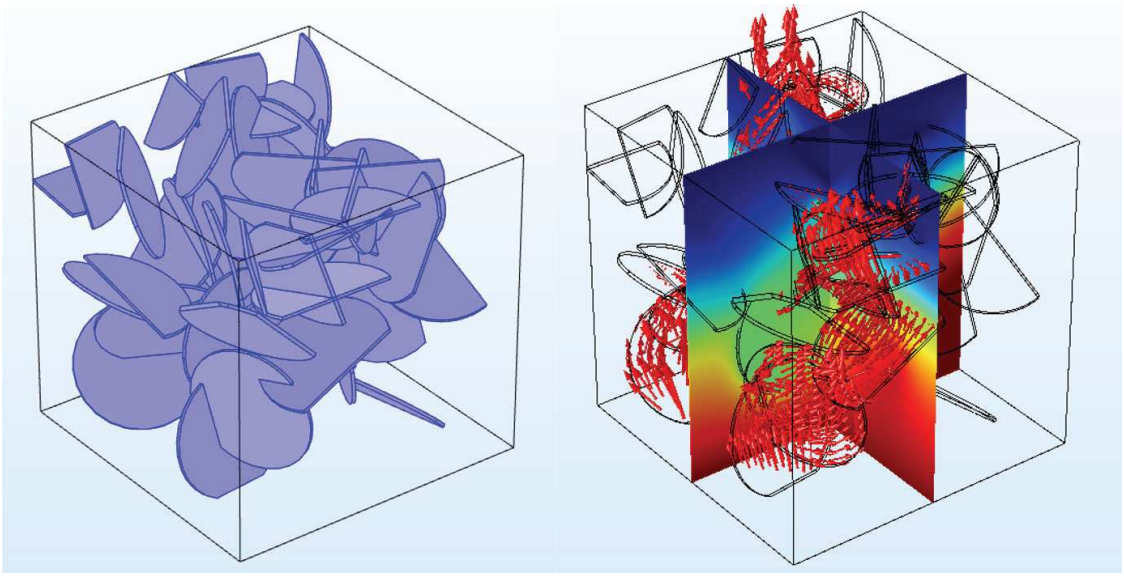

Fig. 13 Left: a 3D isotropic Poissonian fracture network with finite size fractures. Right: representation of the hydraulic head on selected planes (color shading) and of the Darcy velocity (arrows) simulated under PBC. The percolating cluster connects top and bottom faces of the domain

ones. It can be seen clearly, by observing the velocity field represented by arrows, that a percolating cluster of fractures relates the two opposite permeable sides. However, determining the critical percolation density using permeameter boundary conditions (PBC) seems to be very limiting because it considers only the largest clusters of fractures (i.e., the clusters connecting two opposite sides). In fact, other types of clusters can connect faces that are not necessarily opposed (Fig. 14 shows an example of a percolating cluster linking two adjacent sides of the three-dimensional domain). These types of clusters can be detected by using instead the "constant heads boundary conditions (CHBC)" as demonstrated in Fig. 14.

To illustrate these differences, concerning the definition of percolation and the types of boundary conditions, the same three-dimensional fracture network of Fig. 14 has

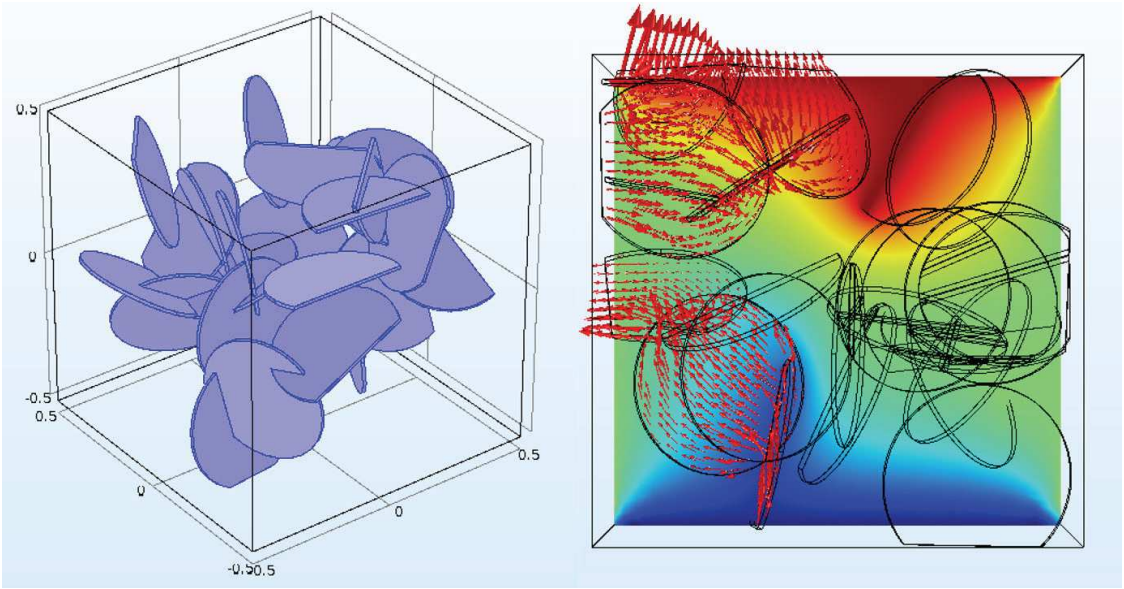

Fig. 14 Left: 3D isotropic network of Fig. 13. Right: an (XY) plane view of a detailed simulation on of flow under CHBC: hydraulic head (color shading) and the Darcy velocity (arrows). The percolating clusters are visible from the velocity field. The percolating clusters connect two adjacent faces

been re-used. The equivalent conductivity tensor has been determined numerically, for an increasing fracture density of this same network under two different types of boundary conditions: (1) PBC and (2) CHBC. The results are presented in Fig. 15. As explained before, percolation can be detected as a sudden increase of $\underline{\underline{K}}_{\mathrm{EQ}}$. The critical fracture density $\rho_{\mathrm{EX},C}$ was significantly different for the two boundary conditions $\rho_{\mathrm{EX},C} \approx 0.6$ for the CHBC, and $\rho_{\mathrm{EX},C} \approx 1.9$ for the PBC (Fig. 15). The example of Fig. 15 concerns a single realization of the three-dimensional fracture network. These observations confirm the fact that constant heads boundary conditions (CHBC) permit the detection of clusters relating any two boundaries of the domain, and therefore, percolation is observed early for non-opposite boundaries (small fracture density). On the other hand, permeameter boundary conditions (PBC) detect only the large clusters relating the two opposite faces of the domain, and therefore, percolation is detected at much larger densities (compared to CHBC).

The identification of the critical density of percolation is a relatively sensitive computational process, and the resulting critical density may be qualified itself as a random variable (over the ensemble of finite domain fracture networks of a given type). This uncertainty has been analyzed qualitatively in two ways:

1. How variable is the critical density $\rho_{\mathrm{EX},C}$?

As can be clearly seen from Fig. 16 (left), the degree of variability of the critical percolation density $\rho_{\mathrm{EX},C}$ is not negligible. This variability can be explained by the fact that percolation (under CHBC) can occur in different ways. For example, percolation can occur if two adjacent boundary faces are connected by a small cluster. This case will be the more frequent for "finite size" fractures (otherwise, percolation could also occur as the consequence of a larger cluster connecting two opposite faces). Hence, when one calculates the critical density, the corresponding critical number of fractures

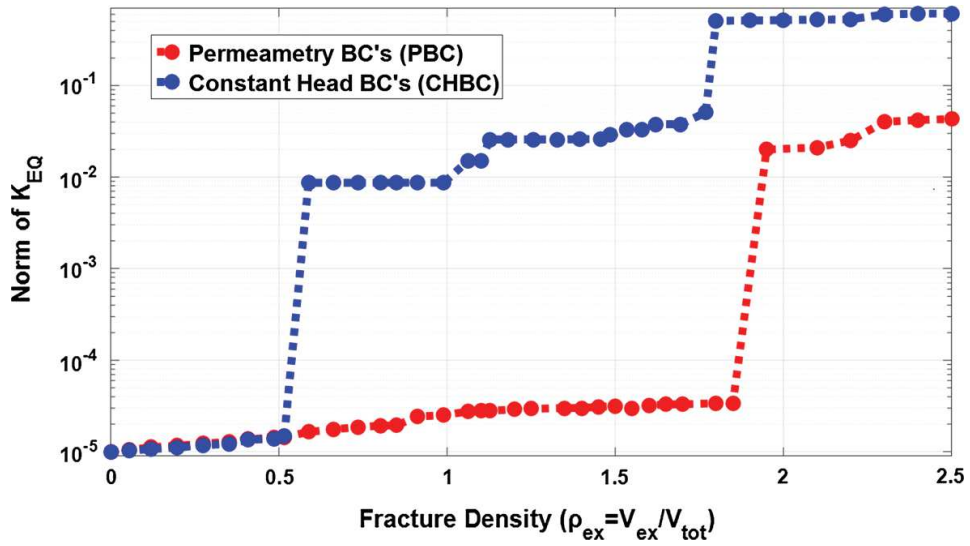

Fig. 15 Example of calculation of $\rho_{EX,C}$ by imposing PBC (red) and CHBC (blue). $\rho_{EX,C}$ corresponds to the density at which a sudden jump of the $\underline{\underline{K}}_{EQ}$ is observed (by 3 orders of magnitudes in this example). The resulting $\rho_{EX,C}$ are different for the two boundary conditions: 0.6 for CHBC and 1.9 for PBC

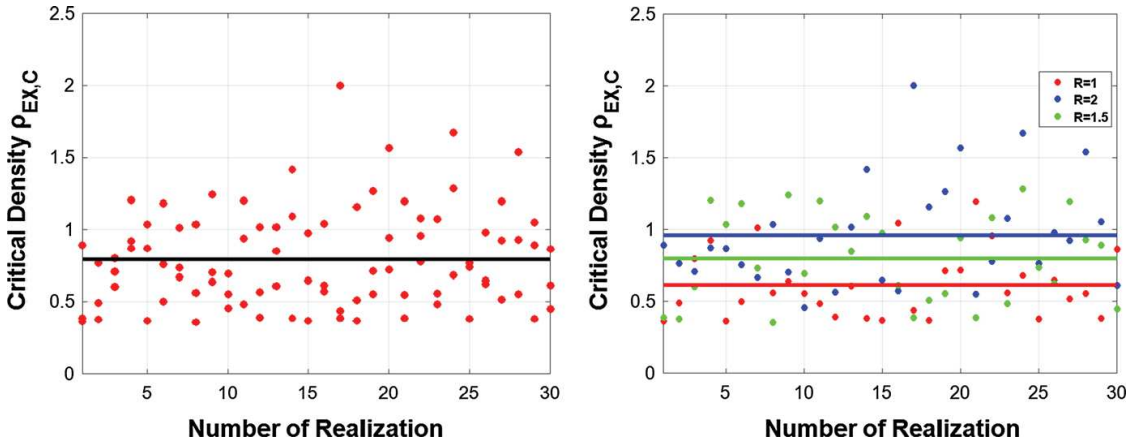

Fig. 16 Critical density ($\rho_{EX,C} = V_{EX,C}/V_{tot}$) for multiple realizations of a three-dimensional isotropic Poissonian fracture network. Left: all realizations combining the 3 radii $R=1.0$, $R=1.5$, $R=2.0$ [m]. Right: same realizations grouped in three sets corresponding to the three fracture radii (with 3 different symbols for $R=1.0$, $R=1.5$, $R=2.0$ [m])

is usually small, and, therefore, a high variability is expected across replicates of the network.

2. Does the critical density $\rho_{EX,C}$ depend on fracture radii?

Figure 16 (right) presents a qualitative analysis of the sensitivity of the critical density with respect to fracture size (radii). The results (Fig. 16 right) were obtained by performing, for different fracture radii, the same procedure for determining $\rho_{EX,C}$ as described earlier at the beginning of this section (Sect. 4.2.2). It can be seen that the critical density increases with fracture radius. This dependence was not revealed on the previously cited results found in the literature, where the critical density of percolation $\rho_{EX,C}$ is stated to be a universal quantity, independent of fracture size distribution (Mourzenko et al. 2005). This size sensitivity is not studied further in the present work; and this topic is kept as a perspective for future investigations. Finally, in the

remainder of this paper, the critical density is assumed to be the mean value obtained from all the realizations in the present work. In conclusion, the critical density to be retained here is found to be $\rho_{EX,C} \approx 0.75$.

4.2.3 Extension of the Superposition Formula for Finite Size Fractures

As mentioned earlier, the hydraulic behavior of the fracture network is radically dependent on the fracture density when fracture diameters are significantly smaller than domain diameter (finite size fractures). Therefore, the critical percolation density ($\rho_{EX,C}$) should play a significant role in the estimation of equivalent hydraulic conductivity. More precisely, it was seen that the increase of fracture density ρ_{EX} does not drastically affect the equivalent hydraulic conductivity as long as fracture density remains smaller than $\rho_{EX,C}$ because, at low density, fractures do not yet form a percolating cluster. When ρ_{EX} reaches the critical density $\rho_{EX,C}$, a percolating cluster of fractures is formed. The increase of fracture density beyond this critical value increases the equivalent conductivity. The fast superposition method, as implemented so far, did not include this critical hydraulic behavior. For this reason, a novel semi-empirical superposition formula is proposed, which would be able to handle a set of finite size fractures for a broad range of fracture density and connectivity. This proposed formula is based on the critical percolation density ($\rho_{EX,C}$) defined in Sect. 4.2.1.

The "fast superposition method" is accordingly modified and extended as follows: for density ρ_{EX} below the critical percolation density ($\rho_{EX,C}$), the fractures do not form percolating clusters. The superposition method is therefore modified to compute the equivalent hydraulic conductivity $\underline{\underline{K}}_{EQ}$ as a harmonic mean over all mono-fracture blocks. This harmonic averaging procedure permits to take into account the hydraulic conductivity of the porous matrix, particularly for non-percolating fracture sets. For density ρ_{EX} over the critical percolation threshold ($\rho_{EX,C}$), a numerical fit between the equivalent hydraulic tensor obtained by numerical upscaling and the one obtained by the initial superposition method of Eq. (14) has been performed, over a large range of fracture densities. Finally a semi-empirical analytical expression for $\underline{\underline{K}}_{EQ}$ is obtained, where the critical density plays an important role.

The procedure is implemented following three steps:

1. First, the equivalent $\underline{\underline{K}}_{EQ}$, tensor obtained either numerically or by superposition, is diagonalized as explained earlier (below Table 1).
2. Then, a search (by a fitting procedure) of an empirical correction factor $f(\rho_{EX})$ that can calibrate the superposition method for densities ρ_{EX} larger than the critical density $\rho_{EX,C}$ is performed. A linear relation is proposed for the empirical correction factor $f(\rho_{EX})$ by

$$f(\rho_{ex}) = \frac{\|K_{\text{numerical}}\|}{\|K_{\text{superposition}}\|} = A\rho_{ex} = 0.68\rho_{ex}, \tag{23}$$

where the fitting was performed by linear regression over a large range of fracture densities (Fig. 17). The result of this linear regression was of the form

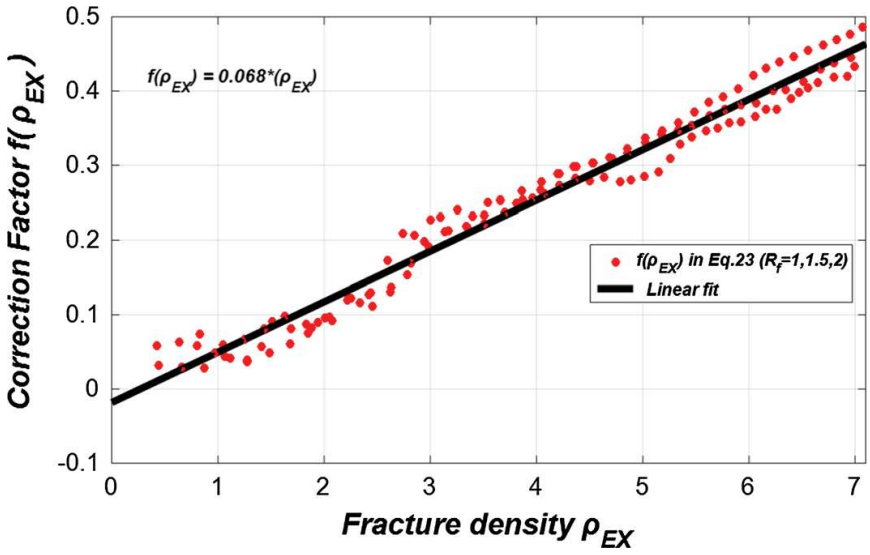

Fig. 17 Linear fit of the correction factor $f(\rho_{\mathrm{EX}})$ as a function of fracture density ρ_{EX}. The linear behavior of $f(\rho_{\mathrm{EX}})$ is roughly the same for different fracture radii ($R = 1.0$ m, 1.5 m, 2.0 m). Determination factor: $R^2 = 0.97$

$$f = AX + B \quad \text{with } B \approx 0. \tag{24}$$

The determination factor is $R^2 = 0.97$, which yields a relative root mean square error $\varepsilon = sqrt(1–R^2) = 0.173$ or 17.3%. This fitting was performed over fracture sets having different fracture radii (constant within each set). It was observed clearly that the correction factor $f(\rho_{\mathrm{EX}})$ depends linearly on fracture density ρ_{EX} in a unique way for all fracture radii (Fig. 17). This confers a "generic" character to the correction factor. In other words, the proposed semi-empirical correction factor is relatively robust. It is worth to note that the linear dependence of $f(\rho_{\mathrm{EX}})$ was observed only for the range of densities studied here

$$0 \leq \rho_{\mathrm{ex}} = \frac{V_{\mathrm{ex}}}{V_{\mathrm{tot}}} \leq 7. \tag{25}$$

Although bounded, this range of density is still relatively large, because it goes from very poorly connected networks to well-connected networks. Larger fracture densities would need more computational capacities and are not studied here.

3. Finally, the *"extended"* fast superposition expression is, therefore, reformulated (for finite size fractures) as

$$\underline{\underline{K_{\mathrm{EQ}}}} = f(\rho_{\mathrm{ex}}) \sum_{f=1}^{f=N_f} \Phi_{\mathrm{bloc}} \underline{\underline{Rot_f}}\, \underline{\underline{K_{\mathrm{bloc}}}}\, \underline{\underline{Rot_f^t}} \quad \text{if } \rho_{\mathrm{ex}} \geq \rho_{\mathrm{ex},c}$$

$$\underline{\underline{K_{\mathrm{EQ}}}} = \left\{ \sum_{f=1}^{f=N_f} \left(\Phi_{\mathrm{bloc}} \underline{\underline{Rot_f}}\, \underline{\underline{K_{\mathrm{bloc}}}}\, \underline{\underline{Rot_f^t}} \right)^{-1} \right\}^{-1} \quad \text{if } \rho_{\mathrm{ex}} < \rho_{\mathrm{ex},c}, \tag{26}$$

where N_f is the total number of fractures in the homogenization domain.

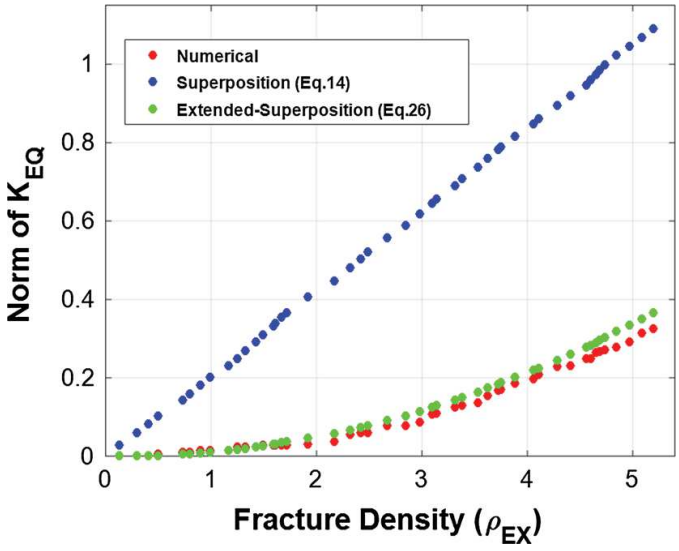

Fig. 18 Comparison of the results of the equivalent hydraulic conductivity as function of the dimensionless fracture density ρ_{EX}. Numerical upscaling (red), initial superposition method of Eq. (14) (blue), and extended superposition method of Eq. (26) (green)

The validity of the above "extended" expression of the superposition method is tested for Poissonian fracture network with isotropic orientation in three dimensions. The size distribution follows a truncated Pareto distribution with lower and upper bound radii, $R_{\min} = 0.5$ m and $R_{\max} = 2.5$ m, respectively. The domain size is $10 \times 10 \times 10\,[\mathrm{m}^3]$; therefore, even the largest fractures are significantly smaller than domain size. The results (Fig. 18) show the relevance of the proposed extended superposition model (Eq. 26) for the range of fracture density studied. The upscaled conductivity results from Eq. (26) represent a very clear improvement of the method compared to the initial version given by Eq. (14). The errors E_1 and E_2 for both superposition methods (the initial version, and the new *extended* version) have been calculated. The errors are calculated as the mean absolute difference between the norm of $\underline{\underline{K}}_{\mathrm{EQ}}$ of reference (obtained numerically) and the $\underline{\underline{K}}_{\mathrm{EQ}}$ calculated by the superposition method. Error E_1 corresponds to the initial superposition method (Eq. 14) and E_2 corresponds to the extended superposition (Eq. 26). Here, the errors are $E_1 = 0.140\ K_F$ and $E_2 = 0.019\ K_F$. The error of the extended method is about seven times smaller than the initial superposition method, for finite non-percolating fractures. Plotting the same results with a logarithmic scale for equivalent conductivity (Fig. 19) allows appreciating the jump in hydraulic conductivity due to the percolation effect on equivalent conductivity. It occurs at a density of 0.51 for the numerical upscaling, and 0.75 for the extended superposition method (Eq. 26). This difference is probably due to the uncertainty on the determination of the critical percolation density, as discussed earlier (Sect. 4.2.2).

4.3 Extension to Mixed Type Networks (Broad Distribution of Fractures Radii)

This section treats a more realistic representation of the porous fractured rock, where both "infinite" and finite size fractures are present. More precisely, the fracture network contains at the same time two types of fractures. The first type of fracture intersects at least two different boundary faces of the homogenization domain, typically, large diameter fractures or faults (labelled "CB" for "connecting boundaries"). The second type of fracture does not connect more than one boundary face of the homogeniza-

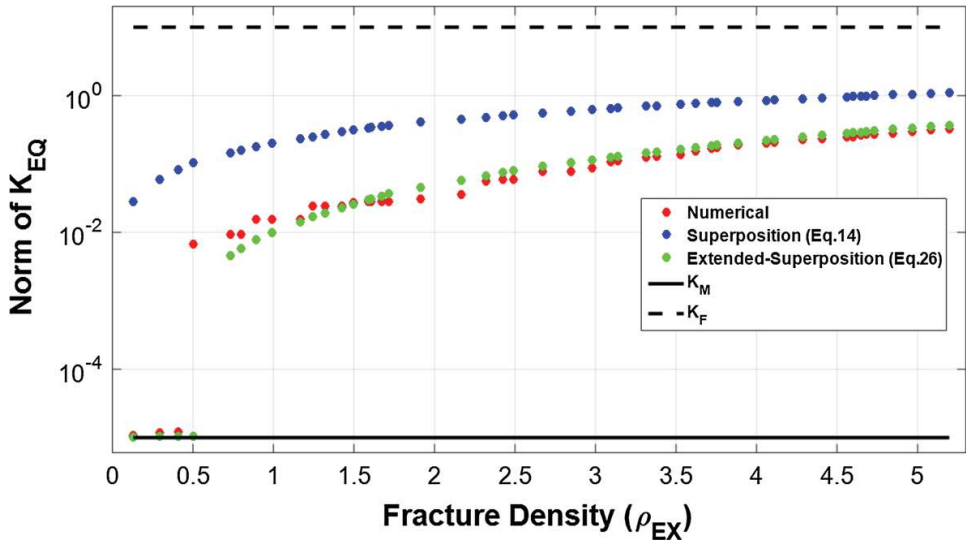

Fig. 19 Semi-log representation of the norm of the equivalent conductivity tensor, as a function of dimensionless fracture density: numerical (red symbols), initial superposition method (blue symbols) and extended superposition method (green symbols). For comparison, matrix and fracture conductivities are also shown: the solid curve represents K_M (matrix conductivity) and the dashed curve represents K_F (fracture conductivity)

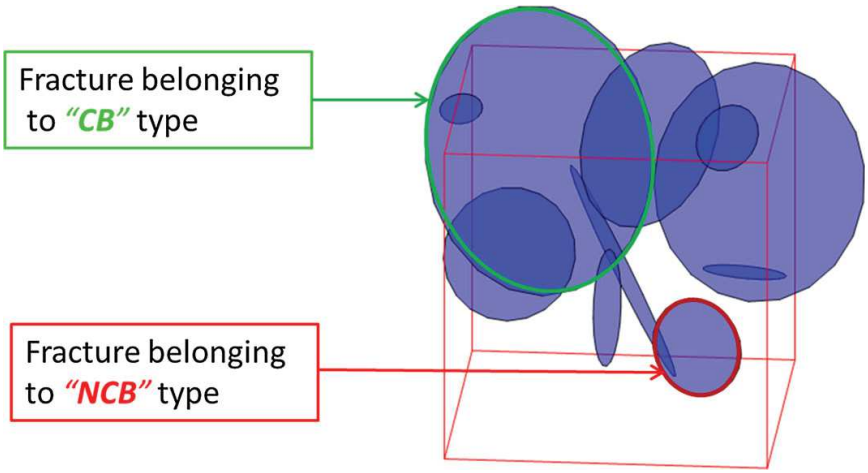

Fig. 20 Representation of the two types of fractures in a mixed network. The red cube is the homogenization domain. The large green fracture belongs to the "CB" type, and its crossing index is $C_f = 3$. The smaller red fracture belongs to the "NCB" type, and its crossing index is $C_f = 0$

tion domain; this includes fractures that do not intersect any boundary at all (this second type is labelled "NCB" for "non-connecting boundaries"). A crossing bounds index, "C_f" is introduced. For each fracture f, "C_f" is the number of intersections of fracture "f" with the boundaries of the homogenization domain. Since the domain is parallelepipedic, "C_f" is a number between 0 and 6 for each fracture. Figure 20 is a schematic representation of the distinction between the two types of fractures ("CB" and "NCB"). The union of CB and NCB constitutes the complete set of fractures.

The aim of this section is to propose a new extended version of the superposition method that can also handle this type of mixed configuration. The new extension works as follows. In the case of a CB fracture ($C_f \geq 2$), this fracture is added to

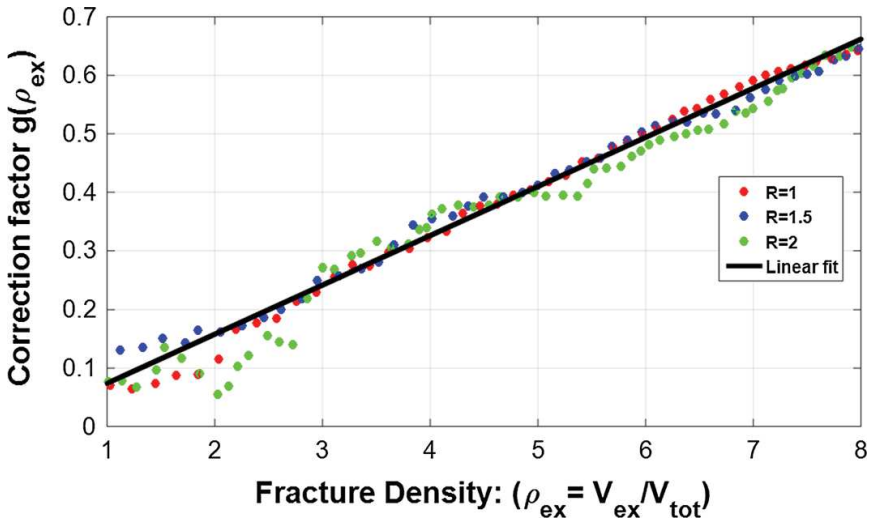

Fig. 21 Plot of $g(\rho_{\mathrm{EX}})$ as a function of the density ρ_{EX}. The linear behavior of $g\ (\rho_{\mathrm{EX}})$ is nearly the same for three different fracture radii: $R=1.0$, $R=1.5$, $R=2.0$ [m]. The determination coefficient is $R^2=0.965$

the superposition algorithm (without any correction factor). In the case of a NCB fracture ($C_f \leq 1$), this fracture is added to the superposition algorithm multiplied by a correction factor $f(\rho_{\mathrm{EX}})$ obtained empirically in a manner similar to Sect. 4.2.3. The new correction factor $f(\rho_{\mathrm{EX}})$ is defined, taking into account differently the CB and NCB type fractures, as follows

$$\left\| K_{\mathrm{EQ}} \right\| = \| K_{\mathrm{CB}} \| + f(\rho_{\mathrm{ex}}) \, \| K_{\mathrm{NCB}} \| \Rightarrow f(\rho_{\mathrm{ex}}) = \frac{\left\| K_{\mathrm{EQ}} \right\| - \| K_{\mathrm{CB}} \|}{\| K_{\mathrm{NCB}} \|}, \tag{27}$$

where K_{CB} and K_{NCB} are, respectively, the equivalent conductivity tensor of the "CB" fractures and of "NCB" fractures, respectively, and $\underline{\underline{K}}_{\mathrm{EQ}}$ is the equivalent conductivity tensor of the entire fracture network. Let us now define another connectivity index "$\rho_{EX,NCB}$" (Eq. 28), which represents the connectivity between the non-crossing fractures (NCB),

$$\rho_{\mathrm{ex,NCB}} = \frac{V_{\mathrm{ex,NCB}}}{V_{\mathrm{tot}}}, \tag{28}$$

where $V_{\mathrm{EX,NCB}}$ is the excluded volume of the "NCB" subset of fractures. The former correction factor of Eq. (27) divided by $(\rho_{\mathrm{EX,NCB}})^2$ as a function of ρ_{EX}, plotted in Fig. 21, is given by

$$g(\rho_{\mathrm{ex}}) = \frac{f(\rho_{\mathrm{ex}})}{(\rho_{\mathrm{ex,NCB}})^2} = A\rho_{\mathrm{ex}} + B. \tag{29}$$

A linear behavior is observed for all the fracture sizes studied here, and this is confirmed by a linear regression fit, as shown in Fig. 21. The relative independence of this linear fit with respect to fracture radius confers a generic character to this linear fit. It is relatively robust, and it can be applied with confidence to various fracture radius distributions, at least in the range of radii investigated here (from 1/10 to 1/5 the size

of the homogenization domain). Hence, the final extended superposition expression for the equivalent conductivity tensor that takes into account the two types of fractures "CB" and "NCB" is

$$\underline{\underline{K_{\mathrm{EQ}}}}(\rho_{\mathrm{ex}}) = \sum_{f=1}^{f=N_{\mathrm{CB}}} \Phi_{\mathrm{bloc}}\, \underline{\underline{Rot_f}}\, \underline{\underline{K_{\mathrm{bloc},f}}}\, \underline{\underline{Rot_f^t}} + g(\rho_{\mathrm{ex}})\,.\,(\rho_{\mathrm{ex,NCB}})^2\,.\, \sum_{f=1}^{f=N_{\mathrm{NCB}}} \Phi_{\mathrm{bloc}}\, \underline{\underline{Rot_f}}\, \underline{\underline{K_{\mathrm{bloc},f}}}\, \underline{\underline{Rot_f}}^t, \tag{30}$$

where N_{CB} and N_{NCB} are the number of fractures in the homogenization domain belonging respectively to "CB" and "NCB" types (as shown in Fig. 20), and $g(\rho_{\mathbf{ex}})$ is a correction factor that depends linearly on fracture density $\rho_{\mathbf{ex}}$, and finally, $\rho_{\mathrm{ex,NCB}}$ is the density of the subset of NCB fractures that do not intersect more than one boundary face.

In order to validate Eq. (30), a three-dimensional fracture network with Poissonian distribution of fracture position and with isotropic orientation has been chosen. The radius distribution is a truncated Pareto law with $R_{\min} = 0.5$ [m] and $R_{\max} = 3$ [m]. The domain of homogenization is a parallelepiped of size $10 \times 10 \times 10$ [m]. The results (Fig. 22) demonstrate a clear improvement in comparison with the initial superposition method (Eq. 14) for the whole range of fracture density studied. The extended superposition method (Eq. 30) predicts the equivalent conductivity tensor with considerable accuracy, at least in terms of its norm. The errors E_1 and E_2 are calculated for both superposition methods: the initial version (Eq. 14), and the new extended version (Eq. 26). The errors are $E_1 = 0.16\ K_F$ for the initial version of the superposition method, and $E_2 = 0.02\ K_F$ for the extended version. Here, the extended method (Eq. 30) yields an error 8 times smaller than the initial superposition method, for a mixed type of network with both percolating and non-percolating fractures.

Finally, it was observed that the typical computation time to obtain the equivalent conductivity tensor $\underline{\underline{K_{\mathrm{EQ}}}}$ by the quasi-analytical superposition method of the synthetic samples studied in this paper (all samples evoked in Sect. 4) was only a few seconds. In comparison, to obtain $\underline{\underline{K_{\mathrm{EQ}}}}$ numerically (by direct simulations and numerical upscaling), the typical computation time was of the order of 30 min. Furthermore, direct numerical simulations are very limiting in practice: (i) the meshing procedure can fail if fracture aperture is very small, and (ii) the CPU time for solving very large algebraic systems may become impractical (typically, the three-dimensional grids may have to involve hundreds of millions of cells).

5 Conclusions

In this paper, a computationally efficient superposition method for upscaling the hydraulic conductivity of a three-dimensional porous and fractured rock sample is proposed. The proposed superposition method is used without recourse to detailed flow simulations except for connectivity and critical density calculations.

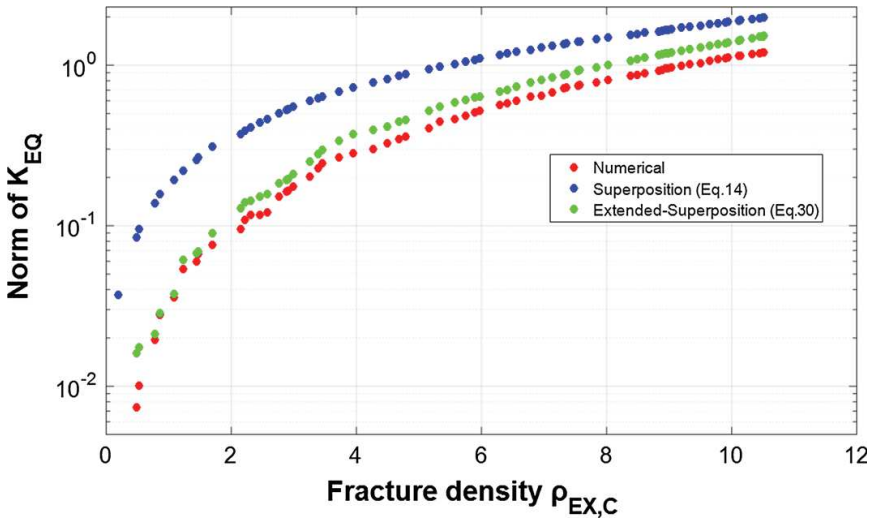

Fig. 22 Semi-log representation of the equivalent hydraulic conductivity norm as a function of the dimensionless fracture density ρ_{EX}. Numerical (red), original superposition method (Eq. 14) (blue) and extended superposition method (Eq. 30) (green)

The superposition method presented in this paper is based on a flux superposition method (Ababou et al. 2011), which was a useful and efficient upscaling tool, but had several limitations: (i) it did not explicitly formulate the conductivity as a volume weighted combination of fracture/matrix conductivities; (ii) the approximate flux superposition yields essentially a weighted arithmetic mean conductivity tensor; and (iii) it did not take into account the connectivity of the fracture network. This initial upscaling method is improved as follows: (i) the volumetric contributions of each mono-fracture block are now explicitly taken into account; (ii) in the case of non-percolating network, the initial superposition is replaced by a volumetric weighted harmonic mean of mono-fracture blocks; and (iii) semi-empirical connectivity factors are introduced as a function of fracture density and of a critical percolation density. This improved upscaling method yields a three-dimensional tensorial equivalent conductivity $\underline{\underline{K}}_{\mathrm{EQ}}$, which represents hydraulically the fractured porous rock as an equivalent continuum. The present upscaling method only requires, for its implementation, the geometry of the fractures (diameters, orientations, and apertures from probabilistic models or fracture set data), and the hydraulic conductivities of the fractures K_F and of the surrounding porous matrix K_M. In addition, approximate connectivity indexes had to be determined semi-empirically by linear regression from numerical flow experiments. These indexes improved the upscaling method for different types of fracture networks embedded in a porous matrix.

For validation and verification of the upscaling by this enhanced superposition method, detailed flow simulations were implemented on a parallelepiped domain (millions of cells). Our numerical upscaling was based on the volume averaged flux as an equivalence criterion, and on particular boundary conditions called CHBC (constant heads boundary conditions), which has been compared to other boundary conditions.

Numerical upscaling, which is computationally demanding, yields an equivalent conductivity tensor to be compared to the faster superposition methods.

Promising results were obtained for the equivalent hydraulic conductivities calculated by the new superposition method in this paper (Sect. 4), for different configurations of fracture networks. The results were in good agreement with those obtained numerically for different fracture radius distributions. Also, these results were obtained for a wide range of hydraulic conductivity contrasts K_F/K_M in the case of "infinite" fractures. On the other hand, for finite size fractures or mixed networks, our study focused on very high K_F/K_M contrasts, and this, for various configurations in terms of fracture sizes and density of Poissonian isotropic networks. Overall, the new *extended* methods (Eqs. 26, 30) yield an absolute error (E_2) seven to eight times smaller than the error (E_1) of the initial superposition method (Eq. 14), relative to the numerically upscaled conductivity used as the reference.

In summary, our partially validated superposition method provides a computationally efficient algorithm for determining the equivalent continuum hydraulic conductivity tensor for a three-dimensional sample of porous fractured rock. This equivalent tensor serves as input for reservoir flow simulation on larger scales in deep geologic formations like geothermal reservoirs.

Several issues remain worth investigating based on the progress results presented in this paper (ongoing work). The main issues are: (i) a more accurate statistical determination of the critical percolation density $\rho_{\mathrm{EX},\boldsymbol{c}}$ (its sensitivity to fracture diameters, and its variability across replicates of random networks); (ii) investigation of denser fracture networks (limited due to computational capacities); and finally, (iii) unifying into a single formulation the various subcases of the new superposition method with its semi-empirical density-dependent factors (finite/infinite fracture diameters; percolating/non-percolating networks; etc.).

Acknowledgements The first three authors wish to acknowledge the financial support of ADEME (France) in the framework of the GEOTREF project "GÉOThermie haute Énergie en REservoirs Fracturés" (www.geotref.org). We thank the anonymous reviewers for their careful reading of the manuscript and for their insightful comments and suggestions.

References

Ababou R (1990) Identification of effective conductivity tensor in randomly heterogeneous and stratified aquifers. In: Bachu S (ed) Proceedings Fifth Canadian–American conference on hydrogeology: parameter identification and estimation for aquifers and reservoirs, Calgary, Alberta, Canada, Sep. 18–20, 1990. Nat. Water Well Assoc., Water Well Journal Publish. Co., Dublin, Ohio, 1990, pp 155-157

Ababou R, Bagtzoglou AC(1993) BIGFLOW: a numerical code for simulating flow in variably saturated, heterogeneous geologic media (theory & user's manual, Version 1.1). Report NUREG/CR-6028, U.S. Nuclear Regul. Commission, Gov. Printing Office, Washington, DC

Ababou R., Renard P (2011) Equivalent permeability tensor in fractured media: an algebraic approach. In: Amaziane B, Barrera D, Mraoui H, Rodriguez ML, Sbibih D (eds) Proceedings MAMERN11: 4th internat. conf. on approx. methods and numer. model. in envir. and natur. resour. (Saïdia, Morocco, May 23–26, 2011). Univ. Granada (2011), ISBN: 078-84-338-5230-4, 2011

Ababou R, McLaughlin D, Gelhar LW, Tompson AF (1989) Numerical simulation of three-dimensional saturated flow in randomly heterogeneous porous media. Transp Porous Media 4(6):549–565

Ababou R, Millard A, Treille E, Durin M, Plas F (1994) Continuum modeling of coupled thermo-hydro-mechanical processes in fractured rock. In: Peters XA et al (eds) Computational methods in water resources. Kluwer Academic Publishers, Netherlands, pp 651–658

Ababou R, Cañamón Valera I, Poutrel A (2011) Macro-permeability distribution and anisotropy in a 3D Fissured and fractured clay rock: 'Excavation Damaged Zone' around a cylindrical drift in Callovo-Oxfordian Argilite (Bure). J Phys Chem Earth (Spec. Issue "Clays in Natural & Engineer. Barriers for Radioact. Waste Confin.": CLAYS 2010, Nantes, 29 March–1st April 2010). 36(17–18):1932–1948. ISSN 1474-7065. https://doi.org/10.1016/j.pce.2011.07.032

Adler PM, Thovert J-F (1999) Fractures and fracture networks. Kluwer Academic Publishers, Dordrecht

Adler PM, Thovert J-F, Mourzenko VV (2012) Fractured porous media. Oxford University Press, Oxford

Balberg I, Anderson CH, Alexander S, Wagner N (1984) Excluded volume and its relation to the onset of percolation. Phys Rev B 30:3933

Bamberger A (1977) Approximation des coefficients d'opérateurs elliptiques, stables pour la G-convergence. Rapport du Centre de mathématiques appliquées, École polytechnique, n° MAP/15

Berkowitz B, Adler PM (1998) Stereological analysis of fracture network structure in geological formations. J Geophys Res [Solid Earth] 103:15339–15360

Bouwer H (1969) Planning and interpreting soil permeability measurements. J Irrig Drain Div, ASCE 95:391–402

Brown SR (1987) Fluid flow through rock joints: the effect of surface roughness. J Geophys Res 92(B2):1337–1347. https://doi.org/10.1029/JB092iB02p01337

Budiansky B (1965) On the elastic moduli of some heterogeneous materials. J Mech Phys Solids 13:223

Cañamón I (2006) Analysis and modeling of coupled thermo-hydro-mechanical phenomena in three-dimensional fractured media. PhD thesis, Institut National Polytech. de Toulouse & Univ. Politécnica de Madrid

Cardwell WT, Parsons RL (1945) Average permeabilities of heterogeneous oil sands. Trans Am Inst Mining Metall Pet Eng 160:34–42

Charlaix E, Guyon E, Rivier N (1984) A criterion for percolation threshold in a random array of plates. Solid State Commun 50(11):999–1002

Dagan G (1979) Models of groundwater flow in statistically heterogeneous porous formations. Water Resour Res 15(1):47–63

Desbarats AJ (1992) Spatial averaging of hydraulic conductivity in three-dimensional heterogeneous porous media. Math Geol 24(3):249–267

Deutsch C (1989) Calculating effective absolute permeability in sandstone/shale sequences. SPE Form Eval 4:343–348

Dimitrakopoulos R, Desbarats AJ (1997) Geostatistical modelling of grid block permeabilities for 3D reservoir simulators. SPE Reservoir Eng 8:13–18

Farmer CL (2002) Upscaling: a review. Int J Numer Meth Fluids 40:63–78

Hashin Z, Shtrikman S (1963) A variational approach to the theory of elastic behaviour of multiphase materials. J Mech Phys Solid 11:127–140. https://doi.org/10.1016/0022-5096(63)90060-7

Journel AG, Deutsch, C, Debarats AJ (1986) Power averaging for block effective permeability: SPE 15128, presented at the 56th California Regeonal Meeting of the SPE, Oakland, California, April 2–4, 1986

Kfoury M, Ababou R, Noetinger B, Quintard M (2006) Upscaling fractured heterogeneous media: permeability and mass exchange coefficient. J Appl Mech (JAM), Trans ASME 73(1):41–46

Kiraly L (1969) Anisotropie et hétérogénéité de la perméabilité dans les calcaires fissurés. Eclogae Geol Helv 62(2):613–619

Lang PS, Paluszny A, Zimmerman RW (2014) Permeability tensor of three-dimensional fractured porous rock and a comparison to trace map predictions. J Geophys Res Solid Earth 119:6288–6307. https://doi.org/10.1002/2014JB011027

Le Loc'h, G (1988) An efficient strategy for combining the permeabilities: practical application on a simulated reservoir. In: Proc. of the 3rd internat. Geostatistics congress, Avignon, Sept 5–9

Li L, Zhou H, Gómez-Hernández JJ (2011) A comparative study of three dimensional hydraulic conductivity upscaling at the macro-dispersion experiment (MADE) site, Columbus Air Force Base, Mississippi (USA). J Hydrol 404:278–293. https://doi.org/10.1016/j.jhydrol.2011.05.001

Long JCS, Remer JS, Wilson CR, Witherspoon PA (1982) Porous media equivalents for networks of discontinuous fractures. Water Resour Res 18(3):645–658

Marchant.J (1977) Sur la résistance équivalente d'un réseau aléatoire de structure irrégulière. CR Acad Sci Paris, t.284, Série B-85:88

Matheron G (1967) Eléments pour une Théorie des Milieux Poreux. Masson et Cie, Paris, p 166
Mourzenko VV, Thovert JF, Adler PM (2005) Percolation of three-dimensional fracture networks with power-law size distribution. Phys Rev E 72:036103
Mourzenko V, Thovert J-F, Adler PM (2009) Proceedings of the international conference on rock joints and jointed rock masses, Tucson, Arizona
Oda M (1985) Permeability tensor for discontinuous rock masses. Géotechnique 35(4):483–495. https://doi.org/10.1680/geot.1985.35.4.483
Oda M (1986) An equivalent continuum model for coupled stress and fluid flow analysis in jointed rock masses. Water Resour Res 22(13):1845–1856
Pouya A, Fouché O (2009) Permeability of 3D discontinuity networks: new tensors from boundary-conditioned homogenization. Adv Water Resour 32:303–314
Pozdniakov S, Tsang C-F (2004) A self-consistent approach for calculating the effective hydraulic conductivity of a binary, heterogeneous medium. Water Resour Res 40:W05105. https://doi.org/10.1029/2003WR002617
Renard P, de Marsily G (1997) Calculating equivalent permeability: A review. Adv Water Resour 20:253–278
Renard P, Ababou R (2009) Relation between the definition and properties of the equivalent permeability tensor in heterogeneous and fractured porous media. In: Amaziane B et al (eds) Proceedings MAMERN 09: 3rd international conference on approximation methods and numerical modeling in environment and natural resources (Pau, France, 8–11 June 2009), Editorial Univ. de Granada, ISBN: 978-84-338-5006-5
Renard Ph, Le Loc'h G, Ledoux E, de Marsily G, Mackay R (2000) A fast algorithm for the estimation of the equivalent hydraulic conductivity of heterogeneous porous media. Water Resour Res 36(12):3567–3580
Sævik PN, Berre I, Jakobsen M, Lien M (2013) A 3D computational study of effective medium methods applied to fractured media. Transp Porous Media 100(1):115–142
Sahimi M (1995) Flow and transport in porous media and fractured rock. VCH, New York
Snow DT (1969) Anisotropic permeability of fractured media. Water Resour Res 5(6):1273–1289
Tsang YW (1984) The effect of tortuosity on fluid flow through a single fracture. Water Resour Res 20:1209–1215
Vanmarcke E (1983) Random fields (analysis and synthesis). The MIT Press, Cambridge
Warren JE, Price HS (1961) Flow in heterogeneous porous media. Soc Pet Eng J 1:153–169
Wen XH, Gomez-Hernandez JJ (1996) Upscaling hydraulic conductivities in heterogeneous media: an overview. J Hydrol 183:ix–xxxii
Wiener O (1912) Abh. Math.-Phys. Klasse Königlich Sächsischen Des Wiss. Leipzig 32:509–604
Zinn B, Harvey CF (2003) When good statistical models of aquifer heterogeneity go bad: a comparison of flow, dispersion, and mass transfer in connected and multivariate Gaussian hydraulic conductivity fields. Water Resour Res 39(3):1051. https://doi.org/10.1029/2001WR001146